Title: Modeling of Infrared-Visible Sum-Frequency Generation Microscopy Images of a Giant Liposome

Short title: IR-VIS SFG liposome imaging

Victor Volkov, Carole C. Perry

Interdisciplinary Biomedical Research Centre, School of Science and Technology, Nottingham Trent University, Clifton Lane, Nottingham NG11 8NS, United Kingdom

ABSTRACT

The article explores the theory of Infrared-Visible Sum Frequency Generation microscopy of phospholipid envelopes with dimensions larger than the wavelength of the nonlinear emission. The main part of the study concerns derivation and accounting for the contributions of effective nonlinear responses specific to sites on the surfaces of a bilayer envelope and their dependence on polarization condition and experimental geometry. The nonlinear responses of sites are mapped onto the image plane according to their emission directions and the numerical aperture of a sampling microscope objective. According to the simulation results, we discuss possible approaches to characterize the shape of the envelope, to extract molecular hyperpolarizabilities, to anticipate possible heterogeneity in envelope composition and anisotropy of the environment proximal to the envelope. The modeling approach offers a promising analytic facility to assist connecting microscopy observations in engineered liposomes, cellular envelopes and sub-cellular

organelles of relatively large dimensions to molecular properties and hence to chemistry and structure down to available the spatial resolution.

INTRODUCTION

Second-order Infrared-Visible (IR-VIS) Sum Frequency Generation (SFG) is the lowest order nonlinear response to probe molecular composition and structure at interfaces (Zhu et al., 1987); (Guyot-Sionnest et al., 1987); (Walker et al., 1997); (Chen et al., 2010); (Xiao et al., 2012). Within the last two decades, IR-VIS SFG has been demonstrated to be a promising tool to address structure under microscopic spatial resolution (Flörsheimer et al., 1999); (Hoffmann et al., 2002); (Cimatu & Baldelli 2006); (Han et al., 2013); (Jang et al., 2013). To answer the experimental progress, recent effort in the theory of SFG microscopy image reconstruction (Volkov, 2014) suggests a computational protocol to calculate and map selected (by polarization setting) nonlinearities of normal modes of terminal methyls to address the surface of a weakly deformed membrane. The selection of the indicated modes is because they are relatively localized and have resonances that exhibit a distinct peak at about 2950 cm^{-1} (Guyot-Sionnest et al., 1987); (Walker et al., 1997); (Schleeger, 2014). The developed here approach assumes that terminal methyls are distributed in well-determined leaflets of a phospholipid bilayer: inter-digitation is not expected in well-hydrated membranes under physiological conditions. Also, it is important, that the results of image modelling for membrane deformations (Volkov, 2014) are correct as long as the dimensions of the deformed structures are less than the wavelength of nonlinear emission.

For example, consider a geometric structure, as shown in Fig. 1A. Whenever we set angle CBA = α_0 to the zero-limit, the curve connecting A and B converges asymptotically with a straight line between these points, |AB|. If we require |AB| to be comparable with the wavelength of SFG, then we may calculate the radius to fulfil the curvature. Specifically, using $\lambda_{VIS} = 800$ nm, one may expect SFG responses of terminal methyl vibrations at the wavelength $\lambda_{SFG} = 650$ nm. For this wavelength, when $\alpha_0 = 1^o \div 10^o$ we may calculate the corresponding radius of a spherical structure R = |AB|/2Sinα_0 $\approx$ 18.6 ÷2 micron. The anticipated size range is characteristic of engineered liposomes (Angelova & Dimitrov, 1986); (Staneva et al., 2004), erythrocytes (Gulliver, 1875), and various cellular organelles.

The purpose of this study is to explore how image modelling may help in the detection and analysis of such structures; under phase matching conditions, accounting for an acceptance angle α according to the numerical aperture of a microscope objective, and under the experimental geometry to detect upward (reflected) and downward (transmitted) images as shown in Fig. 1B. In the case of a flat interface, we may satisfy the k-vector condition by $\frac{\lambda_{VIS}}{\lambda_{IR}} sin[\beta_2] + sin[\beta_1] = 0$: a pair of angles $\beta_1 \neq \beta_2$ would provide a non-degenerate geometry. When $\beta_1 = \beta_2 = 0$, the direction of the emitted SFG field is not sensitive to the wavelengths of the visible and infrared radiations, and the experiment converges to that reported recently (Han et al., 2013). Under such geometry, an imaging experiment on flat surfaces and on relatively small spherical structures loses the capacity to report on contributions of nonlinearities stimulated by Z components of the mixing fields. The situation is more complex, however, when dimensionality of a structure is comparable or larger than the indicated threshold for the radius of the local curvature. In such case, we have to recognize that every spot has own phase-matching condition. Additionally, it is desirable to develop a

methodology that would account for that cellular structures being multilayered, complex in shape and in composition. To address this, the article suggests a 6-step protocol and considers a 2 micron radius spherical liposome as a model system to test image reconstruction. In the results, the article provides examples of reconstructed images calculated accounting for local phase-matching, different geometries, polarizations of the mixing fields and microscopy sampling conditions.

The outline of the article is as follows: first, relevant nonlinear susceptibilities are derived under assumed orientation averaging. Second, a protocol is provided to reconstruct images of a spherical liposome with dimensions comparable to the employed wavelength. Third, the article addresses liposome shape characterization and possible extraction of single molecular hyperpolarizabilities. Finally it explores polarization settings, which could possibly be helpful in a temperature jump experiment to probe relative arrangement of matter about the interface of the envelope.

COMPUTATION AND METHODS

Quantum Mechanical Studies and Orientational Averaging

Since we address relatively large structures, where every site may have its own local phase-matching conditions, we need to account contributions of all 27 nonlinearities (Zhu et al., 1987); (Kleinman, 1962); (Dailey et al., 2004); (Moad & Simpson, 2004). Here, we employ a restricted B3LYP functional (Becke, 1988); (Lee et al., 1988), and 6-311++g(d,p) basis sets, as implemented in the Gaussian 09 package (Frisch et al., 2010), to anticipate molecular properties. The eigen-modes of the Hessian matrix allow anticipating non-resonant Raman tensors as third derivatives of the energy, d^3E/dF^2dR, where F is the external dipole field and R is the Cartesian coordinates.

However, since the considered nonlinear process employs, first, an infrared field to excite a specific normal mode, and then visible radiation to stimulate the consequent Raman, we employed the IOp(7/33=1) protocol of Gaussian to extract dipole moment and polarization derivatives about the normal modes of interests and used this to express the nonlinearities specific to the modes of terminal methyl groups in dependence on the orientation angles. In particular, Fig. 2 provides the indicated nonlinearities of interest according to the $\{\Theta,\Phi\}$ angular dimensions of the considered spherical structure. The results are according to averaging: about handedness, about modes, which contribute into the same spectral region, and about the types of the rotomers: see Appendix A, and the previous study (Volkov, 2014). In the case that where conical distribution in orientation at a local cite is considered, modelled a microscopy image would experience smearing according to the angle of the conical openings. The impact on orientational averaging, however, would depend on the location of a site. To make it clear, the article provides red and blue contours in χ_{xxx} angular dependence in Fig. 2 to encircle the angular regions according to the distributions at the two sites, shown Fig. 1D (colours of the contours correspond). Current work addresses the case, when a backbone orients strictly along the local z-axis: in result, for each site at the interface, we describe a single amplitude entry in each angular map as in Fig. 2.

<u>Image reconstruction protocol</u>

Under the non-degenerate geometry (when $\beta_1 \neq \beta_2$ in Fig. 1B), for P and S polarizations, the amplitudes of the visible are $\{Cos\beta_2, 0, Sin\beta_2\}$ and $\{0, 1, 0\}$ in respect to the laboratory frame. Analogously, the corresponding amplitudes of the infrared radiation are $\{-Cos\beta_1, 0, Sin\beta_1\}$ and $\{0, 1, 0\}$. In the case of the degenerate geometry (when $\beta_1 = \beta_2 = 0$), for P and S polarizations, the amplitudes of both fields are $\{1, 0, 0\}$ and $\{0, 1, 0\}$, respectively. Knowing the fields' amplitudes, it is

straightforward to model images either for spherical envelopes of radius smaller than 2 microns or for idealistic spherical caps, as accomplished earlier (Volkov, 2014). In contrast, when for a giant liposome, we have to re-express the effective nonlinearities, thus the image modelling protocol consists of the following six steps:

1. We have to suggest a surface reconstruction with a mesh of proper dimensions. Consistently, each local area at the meshed surface would have its own unique set of nonlinear responses. In the case of a spherical structure, one may consider a square grid pattern to mesh the surface. A mesh-patch would be centred at a site n at a distance R_n from {0, 0, 0}, and with its own local coordinate system {x, y, z}$_n$. We may prepare this local coordinate systems transforming the laboratory frame by a corresponding (to the site) set of rotation angles $\{\widetilde{\Theta}, \widetilde{\Phi}\}_n$. Each site would contain a set of molecules under a certain orientation in respect to the local frame and in respect to the laboratory frame: see conical openings in Fig. 1D and the corresponding red and blue encircled areas in Fig. 2. In general, to describe this, one would have to assign to each site a certain subset of molecular orientation angles $\{\Theta_i, \Phi_j$ and $\Psi_k\}_n$ and their variances $\{\pm\delta\Theta_i, \pm\delta\Phi_j, \pm\delta\Psi_k\}_n$ expressed with respect to the lab-frame. The correspondence is not trivial. This may include averaging within the contoured areas (in Fig. 2) according to the conical openings (Fig. 1D). In such a case, we may expect Θ_i - Φ_j angular correlations. Hence, the subscript indexes i, j and k help to predetermine contributing angular combinations for each site. Further, this work considers all molecules to orient perpendicular to the surface of a local site ($\pm\delta\Theta_i = 0^o$), while $\delta\Psi_k$ about a local z-axis is $\pm180^o$. Under these conditions, rotation of the laboratory frame to express a local coordinate system coincides with the rotation to orient a molecule at the site of interest: $\{\widetilde{\Theta}, \widetilde{\Phi}\}_n = \{\Theta, \Phi\}_n$. The expressions of nonlinearities would be according to the angular range $\{\pm\delta\Theta, \pm\delta\Phi\}_n$ characteristic of the boundaries of the mesh-patches. Here, $\delta\Theta$ is not the same as $\delta\Theta_i$, as mentioned earlier: $\delta\Theta$

describes the angular variance of the normal to the surface specific to the meshed patch, while $\delta\Theta_i$ would address a possible contribution from a contoured subset in Fig. 2, if a conical opening is considered.

2. At an arbitrary local site, n, we have to consider each (infrared, visible and SFG) field to have its own (local) plane of incidence (or emission), formed by the local z-axis and the corresponding k-vectors. These affect the field factors (Hirose et al., 1992); (Zhuang et al., 1999); (Li et al., 2011) and the transmission coefficients according to Snell's law (Hecht, 2002) and Maxwell equations (Li et al., 2011). Each field would have its own set of factors. How to account for this? The previous step describes the preparation of the local coordinate system $\{x, y, z\}_n$ by a proper rotation of the Lab-frame with $\{\Theta, \Phi\}_n$. Now, let us recall that the incident visible and infrared fields have their own k-vectors. We may re-express such within the local frame of the site taking projections of each k-vector onto the $\{x, y, z\}_n$ frame. Local x and z projections of each k-vector (of each field) form their own incident plane. Further, we may normalize the two projections of the infrared beam to receive the local "incident plane" associated with x'_{IR} and y'_{IR} axes for the infrared. In result, we may form a corresponding system taking the cross-product: $\vec{y}'_{IR} = \vec{z}'_{IR} \times \vec{x}'_{IR}$. Analogously, we may construct the local "incident plane" (or local effective) system for visible radiation. Also, using the locally projected components of the mixing fields' k-vectors, it is possible to calculate four SFG directions according to the following sums: $\vec{k}^t_{IR} + \vec{k}^t_{VIS}$, $\vec{k}^t_{IR} + \vec{k}^r_{VIS}$, $\vec{k}^r_{IR} + \vec{k}^t_{VIS}$, $\vec{k}^r_{IR} + \vec{k}^r_{VIS}$, where r and t superscript indexes indicate the reflected and the transmitted fields, correspondingly. Each of them would have its own plane of emission, which we may form following the same prescription, as in the case of the visible and the infrared radiations. Therefore, at any local site, n, we may construct six local effective coordinate systems associated with their own incidence and emission planes: $(x'_{IR}, y'_{IR}, z'_{IR})_n$, $(x'_{VIS}, y'_{VIS}, z'_{VIS})_n$, $(x'_{SFG,rt},$

y'$_{SFG,rt}$, z'$_{SFG,rt}$)$_n$ and alike. Since we know the polarization vector of an incident (or of an emission) field at the site n in respect to the laboratory frame, then we can take its projections onto the local incidence (or emission) coordinate system specific to this field, and multiply the projections with the corresponding field factors. The resultant components would report on the effective amplitudes of the field according to the local geometry of the selected site n.

3. We have to develop a geometric criterion to sort local sites to be on the "bright" and on the "shadow" sides for both, IR and VIS radiations. These are necessary to calculate nonlinear responses for a site in a shadow: we have to know both amplitude and polarization of each field, which is transmitted to the site in the shadow through a certain site at the bright side. Properties of the transmitted field are altered according to the local geometry at the site of transmission. Hence, for every site in the shadow, we have to determine a corresponding site on the bright side. There are several ways to accomplish this. This article adopts the following approach. In the considered geometry of the experiment, we may adopt reference vectors for IR and visible fields as $-\vec{\mathbf{k}}_{IR} = \{-Sin\,\beta_2,\,Cos\,\beta_2\}$ and $-\vec{\mathbf{k}}_{VIS} = \{Sin\,\beta_1,\,Cos\,\beta_1\}$ according to the angles as shown in Fig. 1B. Let us consider that we may take a vertical slice through a spherical structure. This we take in a way that both incident vectors (of the infrared and the visible) would be parallel to the plane of the slice. The slice would be a two-dimensional vector space with $\vec{x}_S$ and $\vec{z}_S$ axes, which are parallel to the X and Z axes of the laboratory frame, respectively. The boundary of this space is formed by the local sites of the spherical structure by the intersection of the slice with the surface of the spherical structure. According to dimensionality, we may describe any site i at the boundary of the slice by the x$_{s,i}$ and z$_{s,i}$ projection of a corresponding pointer (vector) in respect to a selected reference "centre" of the slice $(0_s, 0_s)$. If we go clockwise along the boundary of the slice, then, for each pair of nearby sites (i and $i + 1$) we may calculate a connecting vector, $\vec{c}_i = \vec{l}_i - \vec{l}_{i+1}$, where

$\vec{l}_i$ is the pointer to the site ($x_{s,i}$, $z_{s,i}$), exploring the data set for the angles between the connecting vectors $\vec{c}_i$ and the field reference vector $-\vec{k}_{IR}$: Fig. 3. Next, let us consider sites i, and $i+1$, as shown in Fig. 3. If the site i provides the connecting vectors $\vec{c}_l$ to be largely parallel to $-\vec{k}_{IR}$, then we adopt the angle between $\vec{z}_S$ axis and the pointer to the site i to be the first reference angle α_1. Analogously, if the site i provides the connecting vectors $\vec{c}_l$ to be largely antiparallel to $-\vec{k}_{IR}$, then we adopt the angle between $\vec{x}_S$ axis and the pointer to the site i to be the second reference angle α_2. The criteria for a site (at boundary of a selected s-space) to be classified as one in IR shadow are that the angle between the pointer from (0_s, 0_s) to the selected site and the $\vec{x}_S$ axis should be smaller than α_2, and the angles between the pointer and the $\vec{z}_S$ axis should be larger than α_1. In the case of visible radiation, the incident vector is different. Hence, we sort a site to be under direct exposure (in the bright side) of visible radiation, if the angles between the pointer to the site and $\vec{x}_S$ and $-\vec{z}_S$ axes are smaller than α_2 and larger than α_1, respectively. Supplementary Material Document provides examples of sorting erythro-profiles, solving for an equilibrium shape as developed by the Mladenov group (Djondjorova et al., 2004). For every site at the shadow side, we have to determine the corresponding site of refraction and transmission at the bright side: this requires searching for the minimal (absolute) angle among those between the transmitted k-vector and the vectors from the transmitted site to all sites on the shadow side. Upon the refraction, the polarization vector of the transmitted field would be altered. This is the subject of the next step.

4. Here, we consider a bilayer to be infinitively thin. The difference of the index of refraction for water and for a membrane is relatively small: no multiple reflections within the membrane are anticipated at any site. Furthermore, in the following analysis, the article does not account for absorption of either infrared or visible radiation upon transmission through the membrane. We

may adopt the following expression to describe the transmitted field components through a site m (subclass of n, at the bright side), in respect to the laboratory frame:

$$\vec{E}_{m,F}^{t} = \{E_{m,F,\mathbf{X}}^{t}, E_{m,F,\mathbf{Y}}^{t}, E_{m,F,\mathbf{Z}}^{t}\}$$

$$E_{m,F,\mathbf{X}}^{t} = \mathbf{Project}[\ T_{m,F,p'}(\text{Project}[\vec{E}_{m,F}, x'_{m,F}] + \text{Project}[\vec{E}_{m,F}, z'_{m,F}])$$
$$+\ T_{m,s'}\text{Project}[\vec{E}_{m,F}, y'_{m,F}], \mathbf{X}]$$

$$E_{m,F,\mathbf{Y}}^{t} = \mathbf{Project}[\ T_{m,F,p'}(\text{Project}[\vec{E}_{m,F}, x'_{m,F}] + \text{Project}[\vec{E}_{m,F}, z'_{m,F}])$$
$$+\ T_{m,s'}\text{Project}[\vec{E}_{m,F}, y'_{m,F}], \mathbf{Y}]$$

$$E_{m,F,\mathbf{Z}}^{t} = \mathbf{Project}[\ T_{m,F,p'}(\text{Project}[\vec{E}_{m,F}, x'_{m,F}] + \text{Project}[\vec{E}_{m,F}, z'_{m,F}])$$
$$+\ T_{m,s'}\text{Project}[\vec{E}_{m,F}, y'_{m,F}], \mathbf{Z}], \qquad\qquad [1]$$

here, subscript index F indicates either a visible or infrared field. $\vec{E}_{m,F}$ is the field vector of an incident radiation according to a selected geometry and polarization. The equations show that, first, we project the polarization vector onto the effective local coordinate system $(x',y',z')_m$ associated with the incident plane of a beam: see step 2 in the protocol. Second, we scale the corresponding field components with the double transmission factors, $T_{p'}$ and $T_{s'}$ derived according to the indices of refraction and the local angle of incidence using definitions as described elsewhere (Hecht, 2002). Third, we project the scaled fields' components onto the axes of the laboratory frame. Following on from this treatment, we may receive a transmitted polarization vector of a field, which would be altered by Fresnel transmission factors. Since the incidence geometry at a local site (of transmission) is unique, the transformation of the polarization vector would be site-specific: with dependence on where it transmits. The supplementary Material provides graphical

examples on how a selected field vector changes in dependence on the sites of transmissions and geometry.

5. To express the nonlinear response from a site of interest in respect to the laboratory frame, we have to scale field components: $\vec{E}$ or $\vec{E}^t$, which arrive to the site according to the local field factors (Sipe, 1981); (Dick et al., 1985); (Felderhof et al., 1987); (Li et al., 2011) particular to the local effective coordinate systems, which are specific to each field. Accounting for this, we may write a site-specific nonlinear field vector by scaling a unit vector $\vec{P}_i$ along a laboratory axis i (either X, or Y, or Z) with an amplitude according to a nonlinearity χ_{ijk} as

$$\vec{P}_{n,ijk} = \chi_{n,ijk}\, E_{n,VIS,j}\, E_{n,IR,k} * \vec{P}_i \,, \qquad\qquad [2]$$

where, indices j and k indicate scaled projections of the mixing (visible and infrared) fields, respectively, onto the laboratory frame. The employed field components are

$$E_{n,F,X} = \textbf{Project}[\, L_{n,F,x'x'}\, \text{Project}[\vec{E}_{n,F}, x'_{n,F}] + L_{n,F,y'y'}\, \text{Project}[\vec{E}_{n,F}, y'_{n,F}]$$
$$+ L_{n,F,z'z'}\, \text{Project}[\vec{E}_{n,F}, z'_{n,F}], \textbf{X}]$$

$$E_{n,F,Y} = \textbf{Project}[\, L_{n,F,x'x'}\, \text{Project}[\vec{E}_{n,F}, x'_{n,F}] + L_{n,F,y'y'}\, \text{Project}[\vec{E}_{n,F}, y'_{n,F}]$$
$$+ L_{n,F,z'z'}\, \text{Project}[\vec{E}_{n,F}, z'_{n,F}], \textbf{Y}]$$

$$E_{n,F,Z} = \text{P}\textbf{roject}[\, L_{n,F,x'x'}\, \text{Project}[\vec{E}_{n,F}, x'_{n,F}] + L_{n,F,y'y'}\, \text{Project}[\vec{E}_{n,F}, y'_{n,F}]$$
$$+ L_{n,F,z'z'}\, \text{Project}[\vec{E}_{n,F}, z'_{n,F}], \textbf{Z}]$$

$$[3]$$

Here, again, subscript F indicates either a visible or infrared field. In these equations, we employ a site-specific $\vec{E}_{n,F}$ field vector, for sites on the bright side. If the site is on the shadow side, then we replace $\vec{E}_{n,F}$ with $\vec{E}^t_{m,F}$ as the field vector, which is delivered to the site n at the shadow side after passing through a determined site m on the bright side. $L_{n,xx}$, $L_{n,yy}$ and $L_{n,zz}$ are the local field factors as described in literature (Sipe, 1981); (Dick et al., 1985); (Felderhof et al., 1987); (Li et al., 2011).

6. At each site, we have two incident fields (IR and VIS) and, hence, four possible SFG directions according to the following vector sums: $\vec{k}^t_{IR} + \vec{k}^t_{VIS}$, $\vec{k}^t_{IR} + \vec{k}^r_{VIS}$, $\vec{k}^r_{IR} + \vec{k}^t_{VIS}$, $\vec{k}^r_{IR} + \vec{k}^r_{VIS}$, where r and t superscript indices indicate the reflected and the transmitted fields, respectively. Each of 27 possible nonlinearities may contribute to these four emitted directions. However, as indicated in step 2, each direction would have its own local emission plane with the corresponding field factors. Hence, using Eq. (2), we may determine four possible signals scaled by their own local field factors (according to each local emission plane) at a site n as

$$\vec{P}_{n,ijk} = \{P_{n,ijk,\mathbf{X}}, P_{n,ijk,\mathbf{Y}}, P_{n,ijk,\mathbf{Z}}\} \tag{4}$$

$$P_{n,ijk,\mathbf{X}} = \mathbf{Project}[\, L_{n,P,x'x'} \, \mathrm{Project}[\vec{P}_{n,ijk}, x'_n] + L_{n,P,y'y'} \, \mathrm{Project}[\vec{P}_{n,ijk}, y'_n]$$
$$+ L_{n,P,z'z'} \, \mathrm{Project}[\vec{P}_{n,ijk}, z'_n], \mathbf{X}]$$

$$P_{n,ijk,\mathbf{Y}} = \mathbf{Project}[\, L_{n,P,x'x'} \, \mathrm{Project}[\vec{P}_{n,ijk}, x'_n] + L_{n,P,y'y'} \, \mathrm{Project}[\vec{P}_{n,ijk}, y'_n]$$
$$+ L_{n,P,z'z'} \, \mathrm{Project}[\vec{P}_{n,ijk}, z'_n], \mathbf{Y}]$$

$$P_{n,ijk,\mathbf{Z}} = \mathbf{Project}[\, L_{n,P,x'x'} \, \mathrm{Project}[\vec{P}_{n,ijk}, x'_n] + L_{n,P,y'y'} \, \mathrm{Project}[\vec{P}_{n,ijk}, y'_n]$$
$$+ L_{n,P,z'z'} \, \mathrm{Project}[\vec{P}_{n,ijk}, z'_n], \mathbf{Z}] \tag{5}$$

Here, $(x', y', z')_n$ belongs to a specific (one of four possible) sum of k-vectors. A signal along each of the four directions would contain the sum of contributions, determined by Eq. (4): $\sum_{i,j,k\,=\,X,Y,Z} \vec{P}_{n,ijk}$. Setting a polarization analyzer, we may select for the S-polarized signal taking a sum for Y-projections $\sum_{i,j,k\,=\,X,Y,Z} \vec{P}_{n,ijk,Y}$ onto the laboratory frame. Under the degenerate geometry, when $\beta_1 = \beta_2 = 0$ (see Fig. 1B), the P-polarization setting of the analyzer would select a sum for X-projections: $\sum_{i,j,k\,=\,X,Y,Z} \vec{P}_{n,ijk,X}$. Under a non-degenerate geometry, when $\beta_1 \neq \beta_2$, the P-polarization setting of the analyzer would deliver a properly weighted superposition of X and Z projections (Zhuang et al., 1999).

Depending on the local geometry of a site, each of the four signals may point upward or downward, considering the direction of the laboratory Z-axis. In fact, Fig. 1B indicates the possibility of simultaneous detection of upward and downward projected images. Accordingly, this article accounts for both, the sorting by direction and the discrimination by the numerical aperture of a microscope objective. It is easy to show that, for an upward emitted image the radial cut-off distance (from the centre of image, which coincides with the centre of spherical structure) is $R \cdot Sin\frac{\alpha}{2}$, where R is the radius of the sphere, and α is the angle, as shown in Fig. 1B. In this work, the analysis adopts α either to be equal to 18° or 38°: with the latter value corresponding to the numerical aperture of a microscope objective, as considered in a previous study (Volkov, 2014).

Fig. 4 shows angular dependences of downward emitted nonlinear signals for the indicated polarization setting under the degenerate geometry, when $\beta_1 = \beta_2 = 0$, and $\alpha = 18°$. Each dependence contains contributions from all 27 nonlinearities. However, under certain polarizations, contributions of some of them would be larger than of the others. This is due to the fact that at a local site the mixing fields would have amplitudes in respect to the local effective

frames according to the orientation of the semi-flat area of the site. For example, S-polarized Field would have a strong y-component in respect to the local frame either at the top or at the bottom of the envelope. The same field would contribute to a strong z-component in respect to the local frame either at the very left or at the very right sides of the envelope. In the two cases, the field would stimulate different nonlinearities with correspondent y and z indexes. Labels in the half-Φ angular maps, at the right side angular dependences, indicate the sites, where the correspondent nonlinearities would be better stimulated (than other 27) by the fields according to indicated polarization settings. For example, we may see that under SSS polarizations, χ_{YYY} dominates at $\Phi = 90^o$ and $\Theta = 45^o$. Yet, χ_{ZYY} and χ_{YZY} terms become significant (compete with χ_{YYY}) in angular regions, when $\Phi \to 0^o$ and $\Theta \to 45^o$. Another feature is that the nonlinear responses from upper ($0^o < \Theta < 90^o$) and lower ($90^o < \Theta < 180^o$) half-spheres differ. This is the effect of alterations of the fields components upon double transmission through the curved sides under the direct exposure.

It is important to mention here that the calculated angular maps of an SSS and PPP pair; and of SSP and PPS signals preserve the 90° Φ-shifted patterns, as present in Fig. 2 and discussed in Appendix A. Therefore, is not a surprise to see obvious similarity of SPP and PSP maps in the angular range: $0^o < \Theta < 90^o$. Analogously, due to $\chi_{YXY} = \chi_{XYY}$, SPS dependence resembles PSS angular map, when $0^o < \Theta < 90^o$. If different, then this is due to the transmission and to the field factors: see Eqs. (3)-(5). The developed protocol allows approaching image reconstruction for a large spherical structure under various geometries and polarization conditions. The next section provides the specific example and discusses possible implications for data interpretation.

RESULTS AND DISCUSSION

Let us translate the angular maps (shown in Fig. 4) for an inner shell of a bilayer of a spherical envelope of 2-micron radius onto an image plane. This would reconstruct images of a not transparent spherical object covered with a single aliphatic layer, with methyl terminals oriented outward. Fig. 5 demonstrates the angular maps of the nonlinear amplitudes for the inner shell to yield upward (columns A) and downward (column C) emissions under the degenerate geometry ($\beta_1 = \beta_2 = 0$); and to yield upward (columns E) and downward (column G) emissions under the non-degenerate geometry ($\beta_1 \neq \beta_2$), when the numerical aperture of a microscope objective determines $\alpha = 18^o$. At the right side of each angular map, there is a corresponding image for the inner shell of a spherical bilayer envelope of 2-micron radius. Panels in columns A and E provide indications on the considered polarization settings, under which the nonlinearities are calculated and images are modelled.

Let us consider the results of imaging in Fig. 5. The angular maps of the signals emitted upwards resemble (in character) the patterns in the angular maps for the same polarization signals but emitted downwards. However, the angular maps of the signal emitted upward is limited to $\Theta \approx [0^o, \alpha]$ and $[180^o - \alpha, 180^o]$ angular regions by the effect of the numerical aperture: here, $\alpha = 18^o$. Thus, the upward emitted images of a liposome structure are limited to relatively small areas, by the radial cut-off distance from centre of image to the peak of the outer rim of amplitudes at $D_c = R \cdot Sin[\alpha/2]$, next to the poles. In contrast, the angular maps sorted in columns C and G, and the corresponding sets of the images (by columns D and H) indicate that the signals emitted downwards are able to report on the structural content in the region about the equator. Column G demonstrates that under the non-degenerate geometry ($\beta_1 \neq \beta_2$, Fig. 1B) the signal may be more intense in some areas of the surface than under the collinear geometry: for

example, one may compare the upward emitted images under the SSS or SPS polarizations. The enhancement is due to the local incident angles. Due to the large angle of infrared radiation towards to the Z laboratory axis (under a non-degenerate geometry), the correspondent angular maps demonstrate a curved distribution in the $\{\Phi;\Theta\}$ angular space: this is specific to the bright-shadow sorting of the sites for infrared radiation. Moreover, projections of the transmitted (through the sites at the bright side) fields onto the laboratory frame demonstrate a complex pattern in sign: for example, notice the striking negative amplitude of the PPP and SPS signals when Φ is about 180°, and $\Theta < 90^o$. In contrast, under the collinear geometry, both, angular maps of the effective nonlinearities and the projections onto the image plane are easier to perceive and compare.

To reconstruct images of a spherical bilayer structure, we need to account the contributions from the outer shells, as well. Figs. 6A-C represent upward and downward emitted images for a spherical bilayer of 2 micron radius under a range of polarizations, as indicated above the panels in the figure. Under all polarization conditions, the images demonstrate the outer rim amplitude patterns. The build-up of the outer rim amplitude is due to two contributions: 1) increment of density of states imaged onto the plane upon approaching the regions of spherical envelopes, which orient more and more perpendicular to the image plane; 2) structural mismatch of contributions of inner and outer shells. When under the degenerate geometry condition (panels B and C), the images are more obvious to rationalise. For example, pairs of the signals SPP and PSP, SPS and PSS consist of responses, which differ due to site-specific Fresnel and local field factors, only. The pair of the SSS and PPP images, as well as, SSP and PPS ones, demonstrate a 90° rotation of amplitude patterns in the image plane. These are consistent with the angular maps in Fig. 5. When under the non-degenerate geometry (Fig. 6, panel A), the results are more complex: first, the

images are not symmetric or anti-symmetric about the Y axis, at X = 0; second, nonlinear angular maps for PPP, SPP and SPS signals show complex patterns due to sign change (Eq. (3)) upon their refraction and transmissions under oblique incidence: see Figs. S2 and S3 in Supplementary Material Document. Since the results under the degenerate arrangement of beams are easier to interpret: it may be more suitable in structural analysis of giant liposomes, red blood cells and similar systems. However, the non-degenerate geometry may help to gain better responses due to the local field factors and may help avoiding an exposure of some regions in the 3D structure, thus setting up a novel opportunity to address transport phenomena (upon crossing bright-shadow borders). In the following, the article addresses the implications of imaging under the degenerate geometry condition, only.

Contributions of Structural Components

Images in Figs. 6 B and 6C indicate that the response from the outer shell (of the 2-micron radius bilayer envelope) determines the amplitudes of the outer rim pattern in both downward and upward emitted images. Contributions of inner shells are noticeable in the internal areas (closer to the centres) of the images. Of course, these are more obvious in the downward emitted images. Another obvious feature is that, overall, the contribution of the upper half of the envelope prevails over that from the lower half. This is expected: upon examination of Fig. 4, one may notice that the angular region for $\Theta \in [0^o, 90^o]$ contains the larger amplitudes than those for $\Theta \in [90^o, 180^o]$. The attenuation of the contributions of the lower half is a result of the fields alterations upon transmission to the sites located in the shadow sides (not under direct exposure). Nonetheless, one may trace some weak signatures, characteristic of the lower half. For example, in PSP and SPS

downward projected images (panels B and C), the contributions of the sites located at the lower half become more prominent in the amplitude patterns in the internal region of the images the more we move from the outer rim toward the centre of the image. In the case of the upward emitted signals, the contributions of the sites located at the lower half may be noticeable, also. For example, we may clearly see a weak modulation in the outer regions in the SSP, PPS and SPS images, sampled under the high numerical aperture: compare the character of the images of the responses in panels B and C.

The increase of the numerical aperture affects downward emitted images slightly. At the same time, the increase of the numerical aperture has a strong effect on the upward emitted images: it widens the radial cut-off range: see Fig. 6C. In this respect, it is interesting to mention that the upward emitted images bring to attention the most helpful implications of the work on image reconstruction for an abstract spherical cap (Volkov, 2014). In particular, the outer rim in the downward detected image reports on the radius of a spherical structure in the equatorial plane. At the same time, the radial cut-off distance from the centre of the image to the peak of the outer rim in the upward detected image provides another measure of the local curvature: $D_c \approx R \cdot Sin[0.5\alpha]$, where α is the acceptance angle according to the numerical aperture of the microscope objective (Fig. 1B). A sequence of such measurements may help probing a liposome as a 3D object.

Envelope Dynamics

Simultaneous detection and comparative investigation of the outer rim patterns in the upward and in the downward emitted signals opens up an interesting opportunity to monitor envelope dynamics. Specifically, since α is according to the numerical aperture, we may

compare the equatorial radius from a downward emitted image, and the local R at measured D_c from a corresponding upward image. These would allow anticipating the departure of a longitude line, which connects the pole with a corresponding point at the equator, along a selected radial direction from the centre of the image. Furthermore, knowing the numerical aperture of a microscope objective, comparing the positions of the maxima of the outer rims in the upward and in the downward emitted images one may predict the departure of the shape of a liposome from an ideal sphere. Of course, considering the relative contributions of the upper and the lower half-spheres, this is an approximate approach: one has to account for possible contributions from the two halves. For example, under either the SPP, or PSP, or SSS polarizations, readings along the Y-axis at X = 0 would indicate more precisely on the curvature of the upper half along such longitude line (see Fig. 4). By taking a series of such upward and downward emitted pairs of images in dependence on time, one may attempt reconstructing the dynamics of the envelope wobbling on a time scale commensurate with the image sampling rate.

Molecular Properties

It is interesting that the upward detected images in Fig. 6, as limited to certain D_c, resemble those modelled for abstract spherical structures with abrupt edges, as reported earlier (Volkov, 2014). In this respect, it is interesting to compare either horizontal or vertical (according to polarization) slices from the upward emitted images and detected under a smaller numerical aperture with images modelled for an idealistic spherical caps of the corresponding dimensions. First, in the case of symmetric envelopes, the vertical and horizontal slices across the centres of the images (as shown in Figs. 6B and 6C) contain combinations of nonlinearities,

which are easier to rationalize. This is because, along these directions, a transformation of the laboratory to a local frame of a site n (by a $\{\Theta,\Phi\}_n$ pair) requires to vary Θ angle only, while Φ would take discrete values 0° (180°) or 90° (270°). In the case of a non-symmetric envelope, this would be possible at certain locations only: where local frames would have one of the local axes, x or y, to be parallel to one of the axes of the laboratory frame. Let us consider the content provided by a vertical or a horizontal slice from Figs. 6B and 6C. With a help of Fig. 4, we may anticipate which direction would be more instructive and which nonlinearity would be the main to contribute. For example, for the SSS and PPP polarizations, it is more helpful to employ the vertical (along the Y-axis image plane, at X = 0) and the horizontal (along the X-axis in image plane, at Y = 0) slices, respectively. In particular, under the SSS polarization, the reading along the positive direction of the Y-axis (this is in the upper half of the image plane) in corresponding to $\Theta \in [0^o, 180^o]$, while $\Phi = 90^o$ in the angular range shown in the correspondent map in Fig. 4. And the reading along the negative direction of the Y-axis (this corresponds to the lower half of the image plane) corresponds to $\Theta \in [0^o, 180^o]$, while $\Phi = 270^o$: see Fig. 4. Of course, the data in Fig. 4 is for the inner shell only, while the slices represent the interplay of the contribution of the inner shell and the opposite sign contribution of the outer shell, which has a larger radius than the inner one. Analogously, under the PPP polarization, the reading along the positive direction of the X-axis (at Y = 0) corresponds to $\Theta \in [0^o, 180^o]$, while $\Phi = 0^o$.

Second, using an objective with a smaller numerical aperture would allow sampling image areas of a liposome, which are closer to the upper and the lower poles. These are more parallel to XY laboratory plane: hence, if sampled, the nonlinear optical response from such area would resemble better that obtained from an idealistic spherical cap (Volkov, 2014), which deviates little from the XY laboratory plane. An increase of the numerical aperture would allow

sampling images (of the outer rims) due to the structural mismatches at the more tilted areas, that are more distantly located from the poles of the liposome. Thus, upward emitted nonlinear optical images under a higher numerical aperture would be more informative and more complex to consider than those detected under a smaller numerical aperture. The response detected under a smaller numerical aperture would resemble more closely the one from an idealistic and minimally deviating from a spherical cap of corresponding dimensions. It is important to notice that employment of a microscope objective with a smaller numerical aperture would give a looser focusing. At the same time, in this work, for the purpose of analysis and deduction, we calculated images under the same high resolution. We discuss the implication of the resolution limit for the proposed extraction of molecular hyperpolarizability at the end of this section.

Third, here, we may extract contributions of the molecular hyperpolarizabilities to the specific slices under the considered polarizations. In particular, Supplementary Material Document provides a Mathematica code to derive, for example, $\sin\Theta$ $\chi_{XXX}(\Theta,\Phi)$ function integrating $\mathcal{G}_{MK}(\Theta_i,\Phi_j,\Psi_k)\mathcal{G}_L(\Theta_i,\Phi_j,\Psi_k)$ about $\Psi \in [0,2\pi]$ according to the theoretical approach reported earlier (Volkov, 2014). For a practical purpose, by setting $\Phi = 0^o$, it is possible to re-express, for example, nonlinearity χ_{XXX} as a function of Θ along the positive range of the X-axis at Y = 0 in the image plane: $(1/2\pi)$ $\chi_{XXX}(\Theta)$. Here, 2π in the denominator takes care of normalization for the Ψ-angle integration, as accomplished in Supplementary Material Document. Table I lists several nonlinear susceptibilities as functions of Θ, considered for the indicated polarization conditions and for the selected values of the Φ-angle. The tabulated entries under the PPS and PSP polarizations, when $\Phi = 0^o$, are given in the angular brackets and are equated to zero. The same is true for the functions under the PSS and SSP polarizations when $\Phi = 90^o$. The meaning of this is that the content of these entries is according to chiral

hyperpolarizabilities: if the right- and left-twisted rotomers or conformers are equally present (the case considered in this article), the functions average to zero. However, if in an experiment a signal is observed, this may be assigned either to the inequality of chiral contributions or to the $\alpha_{xz}\mu_Y - \alpha_{yz}\mu_X$ contribution of a molecular species, under study. The entries under the PPS and PSP polarizations, when $\Phi = 90^{\circ}$, report on $\alpha_{xx}\mu_Z + \alpha_{yy}\mu_Z$ and $\alpha_{xz}\mu_X + \alpha_{yz}\mu_Y$ superpositions, respectively. These are the same for the SSP and PSS polarization settings, when $\Phi = 0^{\circ}$. In principle, each of the slices is informative for a corresponding pair of molecular hyperpolarizabilities. However, it is possible to extract the $\alpha_{zz}\mu_Z$ component, specifically. In order to do this, we need to combine results of measurements using three different polarizations. For example, for a relatively small numerical aperture objective, we may assume that an upward emitted image is close to that from a spherical cap. Hence we may extract a function along a desired (X or Y) directions using one of the four possibilities:

$$A(X) \sim \frac{1}{Sin\theta} \left(\frac{4}{L_{xyy}} PSS + \frac{2}{L_{yyx}} SSP \right)_{X,Y=0} \tag{6}$$

$$A(X) \sim \frac{1}{Sin\theta} \left(\frac{4}{L_{yxy}} SPS + \frac{2}{L_{yyx}} SSP \right)_{X,Y=0} \tag{7}$$

$$A(Y) \sim \frac{1}{Sin\theta} \left(\frac{4}{L_{xyx}} PSP + \frac{2}{L_{xxy}} PPS \right)_{Y,X=0} \tag{8}$$

$$A(Y) \sim \frac{1}{Sin\theta} \left(\frac{4}{L_{yxx}} SPP + \frac{2}{L_{xxy}} PPS \right)_{Y,X=0} . \tag{9}$$

Here, the subscript index *Y,X=0* indicates that we consider an image slice along the Y-axis at X = 0. For a weak curvature spherical cap and under the degenerate experimental geometry, for example, the local field function L_{xyy} (and similar) would be a number with a little effect. Taking the readings along positive direction of the Y-axis at X = 0 (correspond to vertical slices at $\Phi =$

90° in Fig. 4) in the images under the SSS, PSP, PPS polarizations, and Eq. (9), we may derive an average $\alpha_{zz}\mu_Z$ molecular hyperpolarizability as a function of the tilt of the long molecular axis from the Z laboratory axis as

$$\alpha_{zz}\mu_Z(Y) \sim [\ \frac{2}{L_{yyy}Sin\theta(1-Cos2\theta)}SSS\ -\ \frac{(1+Cos2\theta)}{2Sin\theta(1-Cos2\theta)}\left(\frac{4}{L_{yxx}}SPP + \frac{2}{L_{xxy}}PPS\right)]_{Y,X=0}\ . \qquad [10]$$

Of course, this is not a trivial angular function, which reflects a dependence of matter distribution in space. However, tentatively, considering that the upward emitted image would report mainly on the structural mismatch at the edge of the surface (where the emit nonlinear photons hit the limit of acceptance by the microscope objective numerical aperture) we may adopt $\theta = \alpha$, according to Fig. 1B. Accordingly, panels A and B in Fig. 7 provide the necessary vertical slices extracted from panels B and D in Fig. 6. With this input, we may employ Eq. (10) to calculate $\alpha_{zz}\mu_Z$ containing functions: see black lines in Figs. 7C and 7D. How far away would these extracts be from the original input numbers? We may compare the results with a model by Gaussian distribution:

$$\alpha_{zz}\mu_Z(Y) = \frac{\alpha_{zz}\mu_Z\ N_{out}}{\sqrt{2*w*\pi}} * \exp\left[-\frac{(Y-D_c)^2}{2*w}\right] - \frac{\alpha_{zz}\mu_Z N_{in}}{\sqrt{2*w*\pi}} * \exp[-\frac{(Y-(D_c-\delta))^2}{2*w}]\ , \qquad [11]$$

where D_c is anticipated from the position of the outer rim in the upward projected image and compared to $R \cdot Sin\frac{\alpha}{2}$ according to the position of the outer rim in the downward projected image; δ is the adopted distance between the layers of the terminal methyl groups of the outer and the inner shells; N_{out} and N_{in} are the numbers of molecules in the gridded strips of the considered edges

(outer and inner); and $\alpha_{zz}\mu_Z$ would be the hyperpolarizability of interest. The red-yellow circled lines in Figs. 7C and 7D demonstrate the modelled outer rim response averaged for all rotamers, $\langle\alpha_{zz}\mu_Z\rangle = 5.11$ (kg/mole)$^{0.5}$ (Å^4/amu). The modelled dependence is in the right amplitude range, though, of course, Eq. (11) describes the effect of the very edge structural mismatch, while the black lines in Figs. 7C and 7D provide responses for the continuous distributions. Also, of course, in the case of a liposome response, the larger departure of $\alpha_{zz}\mu_Z$ functions from the dependence by Eq. (11), is due to the more complex nature of the response: there are several nonlinearities to contribute, each with its own local field factor.

Practical extraction of a single hyperpolarizability concerns a number of issues. Spatial resolution would not be an issue in detection of structural properties of an envelope when its radius is larger than 2 microns (Angelova & Dimitrov, 1986); (Staneva et al., 2004). However, a higher resolution would be desirable to address fine features as shown in Fig. 7. The vertical bars (with green diagonal and blue anti-diagonal patterns) represent the data points as depicted by the black line in Fig. 7D but rendered on the grid of 350 nm – the resolution limit possible in conventional microscopy for this wavelength. The bars with the two different patterns demonstrate possible spatial oversampling, when the grid is shifted either due to sample or focus repositioning. Employment of a small numerical aperture objective (this is implied when discussing the results anticipated an objective with the acceptance angle $\alpha = 18^o$) would not allow a desired quality resolution as a small numerical aperture objective give loose focusing. The extraction should be possible with an objective with the acceptance angle $\alpha = 38^o$ or better. Another practical issue concerns fitting of the detected signatures. The model adopts the δ parameter as the separation between layers, assumes a certain departure from spherical shape, and the number of molecules involved in responses (note N_{out} and N_{in} in Eq. (11)). However, the

attractive side of the technique is that with several polarizations it may report on several responses, which have to be consistent with each other, and the adopted parameters may be optimised to yield a reference value for the hyperpolarizability. The outlined approach may be particularly valuable to report and quantify if the non-uniform chemical composition and/or density are present at the interfaces of spherical structures.

Temperature Jump Experiment

A temperature jump experiment provides a sensitive way to probe energy flow pathways, the matter of assembly and coupling of selected normal modes to the environment. An experiment relies on observations specific to the redistribution of populations upon either a direct energy investment into the modes of solvent (Callender & Dyer, 2002), or upon a relaxation after an electronic excitation of a dye molecule (Phillips et al., 1995).

There are three experiments to consider. First, we may rapidly increase the temperature outside. Terminal methyl groups are located in the middle of the bilayer, at the junction of two leaflets (or shells). However, the aliphatic tails (terminated by methyls), as constituent elements, protrudes towards their own (outer or inner) environments. Quantum studies (conducted here) indicate that normal modes of methyl groups are sensitive to the conformational states of aliphatic tails. Hence, in a sense, the normal modes of methyls would respond as infrared chromophores to report on populations (and their redistributions) of conformers within each shell. If the outer environment becomes hotter, then, in the outer shell, aliphatic tails' rotomers would become equally possible (the higher temperature limit of the Boltzmann distribution). In result, for a while, the optical response of the methyl modes of the outer shell would be different from that of the moieties in the inner shell. Appendix B provides the details on the temperature

difference (response at 700 K minus that at 300K) effective nonlinearities for the outer shell. This temperature range is attainable at the surface of a metallic nanostructure upon an excitation of a plasmon. According to the anticipated temperature difference effective nonlinearities, Fig. 8A demonstrates such non-equilibrium temperature jump images (under the indicated polarizations), when conformers in the outer shell become equally possible (hot state), while the all-trans conformer persists to be slightly more probable in the inner shell (cold state). Relaxation of such responses (upon thermal equilibration) would be informative on the energy transfer across the bilayer. In the case, when the inner shell is prepared to be hotter than the outer one, the images would be of opposite signs and slightly smaller in radius, correspondently. For example, this is what one would expect after a uniform excitation of solvent both, inside and outside: the outer shell would cool faster. Imaging dynamics of such signals would report on anisotropy of the environment and on the structural heterogeneity of the liposome, if present.

According to the second scenario, one would slowly change temperature of the whole sample holder to reach the alternative state adiabatically. Then, calculating the difference between the measurements before and after the temperature change would provide images as calculated and reported in Fig. 8B. These would be according to adiabatic temperature difference experiment.

The third relevant experiment would employ an electronic excitation of a single chromophore associated with a membrane with monitoring of the development of a dissipating (from the chromophore) heat wave in the plane of membrane. To rationalize the process, one would have to have images, as demonstrated in Figs. 8A and 8B. These instruct which polarization scheme may be more helpful to sense a temperature change, and in which compartment of a bilayer envelope. For example, we may see that under the PPP polarization, the images (upward and downward) provide the highest sensitivity to the temperature jump. Thus, this polarization may be considered to test the sensitivity of the experiment in general. However, mainly, the responses would be from the upper half-sphere. At the same time, the

contribution of the weaker signal from the lower half would not be distinguishable in the image plane. Additionally, under this polarization, the downward emitted image would not help to determine if the response originates from the area next to the equator or from somewhere else. The same lack of resolving capacity is present in the weaker responses under the SSS, SPP and PSS polarizations. In contrast, the images (upward and downward) under the SSP and PPS polarizations are more specific. The downward emitted image under the former polarization would report on the response from the area next to the equatorial plane and mainly from the upper half. At the same time, both, the downward and the upward collected images of the latter polarization would be informative on the region next to the lower pole of the structure. Let us consider the results under the PSP polarization. The downward emitted image shows the non-equilibrium heat responses from the upper half area next to the equator and from the area next to the lower pole as the outer rim signature and the quartet of spots next to the centre of the image, respectively. In contrast, the upward emitted image reports (indistinguishably) on responses from the areas proximal to both poles together. The last polarization, we wish to consider here is SPS: the downward emitted image provides the heat responses from the equatorial areas of the upper half, while the upward projected image reports (indistinguishably) on the response from the areas proximal to both poles together.

Measurements of heat transport both across a membrane and in-plane with the membrane while imaging the whole envelope would require a corresponding time resolution. As an example, it was experimentally measured that heat transfer from water to the carbonyl moiety of a phospholipid molecule when present in membrane fragments occurs within a hundred picoseconds, with the rate depending on hydration, (Volkov et al., 2006). Considering a cascade of inter- and intra-molecular transfers if across a membrane, it is instructive to take tens of nanoseconds for a heat-front propagation across a membrane as anticipated by using non-equilibrium molecular simulations (Potdar et al., 2015). Additionally, it was anticipated in the group in Sendai (Nakano et al. 2010) that the in-plane heat conduction is 2.5 times

smaller than that across of a phospholipid membrane. The time scale is already within the sampling rate of 17 MHz of the iXon Ultra 897 from Andor, Oxford Instruments. Recently, SPADnet silicon sensors were employed to image with sensitivity down to single photons and under a temporal resolution of 50 picoseconds (Gros-Daillon et al. 2013). A systematic advance in contemporary detection systems provides strong promise for the quantitative sampling of non-equilibrium heat transport events with a microscopy resolution.

CONCLUSIONS

The article addresses IR-VIS SFG microscopy image reconstruction for a three-dimensional spherical system of radius larger than the wavelength of the emitted radiation such as a liposome. The theory of imaging reconstruction is developed for the phase-matched signals under two, non-degenerate (when infrared and visible beams are focused separately) and collinear (degenerate) geometries. The results show that, while the latter geometry is better for a direct and quantitative analysis, the former may be beneficial if some areas of the surface are considered to be unexposed to light. The simulations indicate that while the upward emitted image is helpful to research within the cut off region next to one of the poles (according to the numerical aperture of the microscope objective), the downward emitted image is informative on all of the structural regions. At the same time, the central region in the downward emitted images is free from the response from the moieties specific to phospholipid membrane, as the contributions of the two leaflets cancel each other. The background free region is larger for a larger structure. This makes the polar regions, monitored under the transmission geometry, to be attractive in research on guest molecular systems. The article suggests a numerically tested

protocol to try extracting averaged molecular hyperpolarizabilities for phospholipid molecules. Finally, the work explores the opportunity of temperature jump experiments when IR-VIS SFG microscopy is a probing tool. The results indicate that the approach could be helpful to characterize the relative arrangement of matter by monitoring thermalization pathways in dependence on localization at the surface since different polarization may specify responses from different regions of spherical envelope. Hence, the study provides a systematic theoretical background for practical characterizations of phospholipid membranes' 3D structural assemblies using the IR-VIS SFG microscopy.

TABLE I. The nonlinear susceptibilities as functions of Θ angle, considered for the indicated polarization conditions and for the selected values of Φ angles. Here, $A = 2(\alpha_{xz}\mu_X + \alpha_{yz}\mu_Y) + (\alpha_{xx}\mu_Z + \alpha_{yy}\mu_Z)$. Terms in angular brackets are equated to zero, as the functions are expected to average to zero in the case where torsional conformers of opposite handedness are equally present. In case of experimental extraction, each hyperpolarizability, as listed, would be averaged for all possible structural states.

	$\Phi = 0^\circ$	$\Phi = 90^\circ$
PPS: χ_{XXY}	$\langle (\alpha_{xz}\mu_Y - \alpha_{yz}\mu_X)\, Cos\theta\, Sin\theta \rangle = 0$	$\frac{1}{2}\left(\alpha_{xx}\mu_Z + \alpha_{yy}\mu_Z\right) Sin\theta$
PSP: χ_{XYX}	$-\langle \frac{1}{2}\left(\alpha_{xz}\mu_Y - \alpha_{yz}\mu_X\right) Cos\theta\, Sin\theta \rangle = 0$	$\frac{1}{2}\left(\alpha_{xz}\mu_X + \alpha_{yz}\mu_Y\right) Sin\theta$
PSS: χ_{XYY}	$\frac{1}{2}\left(\alpha_{xz}\mu_X + \alpha_{yz}\mu_Y\right) Sin\theta$	$\langle \frac{1}{2}\left(\alpha_{xz}\mu_Y - \alpha_{yz}\mu_X\right) Cos\theta\, Sin\theta \rangle = 0$
SSP: χ_{YYX}	$\frac{1}{2}\left(\alpha_{xx}\mu_Z + \alpha_{yy}\mu_Z\right) Sin\theta$	$-\langle \left(\alpha_{xz}\mu_Y - \alpha_{yz}\mu_X\right) Cos\theta\, Sin\theta \rangle = 0$
PPP: χ_{XXX}	$\frac{1}{4}\left(A + 2\alpha_{zz}\mu_Z + (A - 2\alpha_{zz}\mu_Z)Cos2\theta\right) Sin\theta$	0
SSS: χ_{YYY}	0	$\frac{1}{4}\left(A + 2\alpha_{zz}\mu_Z + (A - 2\alpha_{zz}\mu_Z)Cos2\theta\right)Sin\theta$

APPENDIX A

We calculate $\chi_{MKL,q}(\Theta, \Phi)$ functions of the relevant normal modes of interest space, as described by Equation A1 for the selected normal modes of decanoic acid (Volkov, 2014):

$$\chi_{MKL,q}(\Theta, \Phi, \Psi) = \frac{\Sigma_{i,j,k} \int_{\Theta_i - \delta\Theta}^{\Theta_i + \delta\Theta} \int_{\Phi_j - \delta\Phi}^{\Phi_j + \delta\Phi} \int_{\Psi_k - \delta\Psi}^{\Psi_k + \delta\Psi} \sin(\Theta_i) \mathcal{G}_{MK}(\Theta_i, \Phi_j, \Psi_k) \mathcal{G}_L(\Theta_i, \Phi_j, \Psi_k) d\Psi_k d\Phi_j d\Theta_i}{\Sigma_{i,j,k} \int_{\Theta_i - \delta\Theta}^{\Theta_i + \delta\Theta} \int_{\Phi_j - \delta\Phi}^{\Phi_j + \delta\Phi} \int_{\Psi_k - \delta\Psi}^{\Psi_k + \delta\Psi} \sin(\Theta_i) \, d\Psi_k d\Phi_j d\Theta_i}, \qquad [A1]$$

where $\Theta \pm \delta\Theta$, $\Phi \pm \delta\Phi$ and $\Psi \pm \delta\Psi$ are the angular ranges about the selected Euler angles to express nonlinearity. Here, each symbol M, K and L represents either X, Y or Z components of the laboratory frame. The first and second functions of the orientation distributions describe the components of the Raman tensor and transition dipole moment of a selected normal mode q: $\mathcal{G}_{MK,q}(\Theta, \Phi, \Psi) = \mathbf{R}_M^t \alpha_q \mathbf{R}_K$ and $\mathcal{G}_{L,q}(\Theta, \Phi, \Psi) = \mathbf{R}_L^t \delta\boldsymbol{\mu}_q$. Here, $\mathbf{R}_M^t = (R_{Mx}, R_{My}, R_{Mz})$ is the row (transposed) vector of the Euler rotation matrix $\mathbf{R}$ about the M axis and α is the Raman tensor. The detailed expression of the Euler rotation matrix (according to the employed notation) is provided elsewhere (Volkov, 2014).

In current study, we adopt $\delta\Theta = 2^o$ to sample the angular range [0°, 180°], $\delta\Phi = 2.5^o$ to sample the angular range [0°, 360°], and integrating Ψ over 2π angular range. These are according to the model and to the dimensions of the adopted mesh for the spherical envelope. Fig. A1 provides the angular dependences for all 27 nonlinearities for mode #115 of the all-trans decanoic acid conformer and of mode #114 of a 120° torsion rotomer (having a higher energy minimum) about the eighth carbon atom of its aliphatic tail.. A reader may notice that the nonlinearities are

invariant upon the exchange of first two (from the left side) indexes, which are specific to the Raman tensors. While among the strongest, χ_{ZZZ} is unique one: its numerical content is unique. In a contrast, the other diagonal nonlinearities: χ_{XXX} and χ_{YYY}, are numerically identical but $\pi/2$-shifted (in respect to each other) about the Φ-angular degree of freedom. We may describe the degeneracy as $\chi_{XXX} = [\chi_{YYY}]_{\Phi,\pi/2}$. Accordingly, with a proper numerical sampling of the Φ-angular space, one may construct χ_{YYY} by a Φ-angular swap of χ_{XXX}. Analogously, we may express other identities as: $\chi_{XXZ} = [\chi_{YYZ}]_{\Phi,\pi/2}$, $\chi_{ZZX} = [\chi_{ZZY}]_{\Phi,\pi/2}$, $\chi_{XXY} = [\chi_{YYX}]_{\Phi,\pi/2}$, $\chi_{XYX} = \chi_{YXX} = [\chi_{XYY} = \chi_{YXY}]_{\Phi,\pi/2}$, $\chi_{XZZ} = \chi_{ZXZ} = [\chi_{YZZ} = \chi_{ZYZ}]_{\Phi,\pi/2}$ and $\chi_{XZX} = \chi_{ZXX} = [\chi_{YZY} = \chi_{ZYY}]_{\Phi,\pi/2}$ which all concern the non-chiral terms. Within the context of this work, a nonlinear susceptibility is considered chiral, whenever its three indices are different from each other.

The decanoic acid rotamer about its 8th carbon atom demonstrates strong chiral nonlinearities: see the lower row in Fig. A1. In contrast, the chiral responses of the all-trans decanoic acid (upper row in Fig. A1) are relatively weak (note the scaling factor of 10 in the figure), and demonstrate a "chess-like" amplitude variances specific to the four quarters according to in-plane rotation by Φ angle. Additionally, in the case of the all-trans molecule, there are several weak features in the chiral angular maps, which indicate on the presence of a slight electronic distortion. In particular, at $\Theta = 90^o$ in $\{\Theta, \Phi\}$ in the angular maps of χ_{YZX} (χ_{ZYX}) and of χ_{XYZ} (χ_{YXZ}) responses, weak diagonal and anti-diagonal "bridging" between the quarters, respectively is observed. When Θ approaches 0° and 180°, the same subtle electronic asymmetry of the backbone contributes to the weak negative and positive amplitudes in the $\{\Theta, \Phi\}$ angular maps of the χ_{XZY} (χ_{ZXY}) and χ_{YZX} (χ_{ZYX}) nonlinearities, respectively. In the case where a backbone lacks any residual twist and asymmetry about its plane, these weak features would not be present and all chiral nonlinearities

would demonstrate an identical "chess-like" variance in amplitude, which would be specific to the four quarters of in-plane rotation by Φ angle. This is principally identical to properties specific to a symmetric top, where off-diagonal components of the Raman tensor are zero.

To understand the contributing role of backbone handedness to chiral nonlinearities, it is instructive to explore responses from structures of opposite handedness. The results for such structures (not shown) demonstrate that the chiral terms to flip about Φ axis (in $\{\Theta, \Phi\}$ angular maps), and change their signs. This effects 6 chiral nonlinearities: $\chi_{XYZ} = \chi_{YXZ}$, $\chi_{XZY} = \chi_{ZXY}$, and $\chi_{YZX} = \chi_{ZYX}$. It is important to mention, that the change in the backbone twist (handedness) affects several such non-chiral nonlinearities $\chi_{XYX} = \chi_{YXX}$, χ_{YYY}, $\chi_{YZZ} = \chi_{ZYZ}$, χ_{XXY}, and χ_{ZZY} as well. For the rotamers of the opposite handedness, these responses would flip about the Φ axis, and change signs, also.

The described angular dependences are consistent with the experimental studies in molecular ensembles at interfaces where Φ angle averaging is likely (Zhuang et al., 1999). Inspection of angular maps shows that Φ integration delivers 3 regular non-zero nonlinearities, that are Θ dependent: $\chi_{XXZ} = \chi_{YYZ}$, $\chi_{XZX} = \chi_{ZXX} = \chi_{YZY} = \chi_{ZYY}$, and χ_{ZZZ}. In fact, the authors of (Zhuang et al., 1999) employed SSP, SPS and PSS measurement to extract χ_{YYZ}, χ_{YZY} and χ_{ZYY} nonlinearities to address structural properties of pentyl-cyanoterphenyl at the air-water interface. The situation is different for the chiral responses. As discussed in the previous section, in the case of a sample with proteins at the interface, any chiral SFG nonlinearity would consist of two contributions: a "chess-like" response according to the Φ specific quarters, and a contribution specific to the backbone handedness. In the case of Φ-averaging, the former contribution averages to zero, the latter one would express according to the nonlinearities. Specifically, under Φ-averaging two nonlinearities $\chi_{XYZ} = \chi_{YXZ}$ reduce to zero, and the other four responses would remain with their relations defined

as $\chi_{XZY} = \chi_{ZXY} = - (\chi_{YZX} = \chi_{ZYX})$. Of course, these four may be detected only if Θ-dependent anisotropy is present. In this respect, the PPS polarization provides the possibility to measure the sum of $\chi_{XZY} + \chi_{ZXY}$, since the χ_{XXY} and χ_{ZZY} components are reduced to zero. Here, the χ_{XZY} and χ_{ZXY} are identical but have different local filed factors (Hirose et al., 1992); (Zhuang et al., 1999); (Li et al., 2011). Under the SPP and PSP polarizations, one would measure the χ_{YZX} and χ_{ZYX} responses, respectively: a reader may left explore discussion elsewhere (Xiao et al., 2012). In case the system consists of both, right and left twisted rotomers of equal probability, all chiral nonlinearities would show the same Φ-dependent chess-order orientational pattern. Upon 360° averaging for Φ angle, their contributions would reduce to zero. However, this may not be the case at the temperature below the phase transition, when relative ordering may bring about formation of domains with a preferred handedness. A confirmation as to whether anisotropy about Φ angle is present would be possible upon measuring the χ_{YYY} contribution under the SSS polarization. In the case of the in-plane Φ-anisotropy, SSS polarization measurement still may fail to report on it: one may observe no signal if it happens that the incidence plane (for the mixing fields) would coincide with the vertical direction in $\{\Theta, \Phi\}$ angular map at $\Phi = 0^o$ and 180°. This may be resolved upon a slight rotation of a sample holder.

Finally, it is instructive to mention that since the numerical degeneracy $\chi_{YZY} = \chi_{ZYY}$ and $\chi_{XZY} = \chi_{ZXY} = - [\chi_{YZX} = \chi_{ZYX}]$, the ratios of the PSS and SPS, PSP and SPP spectra are the functions of media refractive indexes at SFG and visible frequencies:

$$\frac{\sqrt{I_{PSS}(\omega_{SFG})}}{\sqrt{I_{SPS}(\omega_{SFG})}} = \frac{L_{zz}(\omega_{SFG}) \, Sin\beta_{SFG} \, L_{yy}(\omega_{vis})}{L_{yy}(\omega_{SFG}) \, L_{zz}(\omega_{vis}) \, Sin\beta_{vis}} \qquad [A2]$$

$$\frac{\sqrt{I_{PSP}(\omega_{SFG})}}{\sqrt{I_{SPP}(\omega_{SFG})}} = \frac{L_{zz}(\omega_{SFG}) \, Sin\beta_{SFG} \, L_{yy}(\omega_{vis})}{L_{yy}(\omega_{SFG}) \, L_{zz}(\omega_{vis}) \, Sin\beta_{vis}} \qquad [A3]$$

$$\frac{\sqrt{I_{PPS}(\omega_{SFG})}}{\sqrt{I_{PSP}(\omega_{SFG})}} = \frac{L_{zz}(\omega_{SFG}) Sin\beta_{SFG} L_{xx}(\omega_{vis})Cos\beta_{vis}+L_{xx}(\omega_{SFG})Cos\beta_{SFG} L_{zz}(\omega_{vis})Sin\beta_{vis}}{L_{zz}(\omega_{SFG})L_{yy}(\omega_{vis}) Sin\beta_{SFG}} \frac{L_{yy}(\omega_{IR})}{L_{xx}(\omega_{IR})Cos\beta_{IR}} \quad [A4]$$

$$\frac{\sqrt{I_{PPS}(\omega_{SFG})}}{\sqrt{I_{SPP}(\omega_{SFG})}} = \frac{L_{zz}(\omega_{SFG}) Sin\beta_{SFG} L_{xx}(\omega_{vis})Cos\beta_{vis}+L_{xx}(\omega_{SFG})Cos\beta_{SFG} L_{zz}(\omega_{vis})Sin\beta_{vis}}{L_{yy}(\omega_{SFG}) L_{zz}(\omega_{vis}) Sin\beta_{vis}} \frac{L_{yy}(\omega_{IR})}{L_{xx}(\omega_{IR}) Cos\beta_{IR}} \quad [A5]$$

Here, β_{SFG} and β_{vis} are the angles between the SFG, visible and IR beams and the Z-laboratory axis, and the L_{zz} factors are not trivial, since they include surface specific refractive indices (Hirose et al., 1992). Considering the relatively weak dependences of the refractive indices in the frequency range of visible and SFG radiations, Eq. (A2) and Eq. (A3) provide functions, which are possible to measure and model. This would be helpful in a practical accounting of L_{yy} and L_{zz} factors according to a geometry. A helpful constraint comes from the fact that functions by Eq. (A2) and Eq. (A3) must be equal. Anticipation of both L_{yy} and L_{zz} factors for the visible and SFG radiations would allow exploration of the spectral ratios as derived in Eq. (A4) and Eq. (A5). Numerical simulations (data not shown) indicate that the relations may help in extraction of the refractive index of media in the infrared spectral range.

APPENDIX B

Thermochemical analysis within Gaussian 09 (Frisch et al., 2010) provides the energies of the relevant conformers according to the subset of partition functions, specific to each case. Accounting for the degeneracy of each kinked molecules, we may anticipate Boltzmann statistics for the conformers (see left side in Fig. B1) for different temperatures. These are comparable to the properties in fluorinated amphiphil molecules (Collazo et al., 1992). The calculated statistics indicate that at the higher temperature limit (for example at 700 K), the rotomers are equally possible. The results in Fig. 2 are according to the high temperature limit: the structural

averaging assumed equal probabilities for all rotomers, but already at 300 K, there is a slight preference for the extended all-trans conformer. This becomes more obvious at 200 K. At the low temperature limit, the all-trans conformer becomes the main structural state. For presentation purposes, this study adopts the weightings of the conformers as expected at 300 K and 700K. Accordingly, the right side in Fig. B1 provides the temperature perturbed effective nonlinearities, as reported under the indicated polarization conditions in Fig. 4. A temperature jump of 400 K is possible at the surface of metallic nanoparticles upon excitation of a plasmon. In case of a smaller temperature range (of 10 − 20 K), the signals, as reported in Fig. 8, would have to be scaled accordingly

FIGURE CAPTIONS

FIG 1. Panel A: geometry of a curved structure. Panel B: non-degenerate geometry of a SFG microscopy experiment. Panel C: Euler rotation angles Θ, Φ, and Ψ describe an orientation of a hydrated all-trans decanoic acid in respect to the Laboratory frame. Panel D: local coordinate systems {x,y,z} received upon rotation transformation of the laboratory frame {X,Y,Z} using rotation angles {Θ, Φ} of {57^o, 225°} and {33^o, 300°}; cones with circular red and blue traces depict possible local orientational distributions.

FIG 2. {Θ, Φ}$_n$ angular dependences of SFG nonlinearities (as indicated on the top of each angular map) averaged for modes 113, 114, 115 of left and right rotomers of decanoic acid under equal probability (high temperature limit). The scale of the colour code bar for the chiral nonlinearities is ten times decreased to vary in the range [-0.5, 0.5]. Red and blue thick line contours in the χ_{XXX} panel depict angular limits of conical openings about z-local axes at the positions as shown in Fig. 1D.

FIG 3. Geometry of a connecting vector along the sites within a selected slice to fulfil a sorting criterion to identify a site to be either on a shadow side or freely exposed to IR radiation.

FIG 4. Downward emitted nonlinear amplitudes of the inner shell of a symmetric spherical phospholipid membrane envelope in dependence on Θ and Φ under the degenerate experimental geometry and at the high temperature limit. The polarization conditions are as indicated in panels. The angular dependences are calculated for microscope objective acceptance angle α =

18$^{\text{o}}$. At the right side of each angular dependence, there is a factorization half-angular (about Φ angle) map, which show main nonlinearities to contribute into the corresponding signals in dependence on the angular pairs $\{\Theta, \Phi\}_n$.

FIG 5. Angular dependencies of the nonlinear amplitudes for the inner shell of a bilayer envelope under polarizations as indicated in column A and emitted upwards (columns A and E) and downward (columns C and G) for degenerate and non-degenerate geometries, respectively. The results of image mapping are at the right of each angular dependence.

FIG 6. Panel A: upward (upper row) and downward (lower row) emitted images when $\beta_1 \neq \beta_2$ for a 2-micron radius bilayer spherical envelope under polarizations as indicated on the top and for a microscope objective acceptance angle $\alpha = 18^{\text{o}}$. Panel B: the same as in panel A, but when $\beta_1 = \beta_2 = 0$. Panel C: Images calculated for $\beta_1 = \beta_2 = 0$, while the microscope objective acceptance angle $\alpha = 38^{\text{o}}$. Panel D: Images of a spherical cap of a 2 micron radius spherical envelope (Volkov, 2014). Radius of the base plane (CB in Fig. 1A) of the cap is tuned to 0.275 nm (see CB in Fig. 1A) to match best the distance of the outer rim detected in the upward emitted images as shown in Panel B.

FIG 7. Panels A and B: vertical slices from the upward emitted images in Fig. 6D along Y-axis at X = 0 under the indicated polarizations. Black lines in panels C and D represent $\alpha_{zz}\mu_Z(Y)$ functions calculated by Eq. (10) according to the slices provided in Panels A and B, respectively. Yellow-red circled lines (in panels C and D) show the response modelled using Eq. (11). Blue diagonal patterned bars demonstrate factorized contribution of $\alpha_{zz}\mu_Z(Y)$ upon rendering the

signals on the grid of 330 nm – the anticipated resolution limit in. Green anti-diagonal patterned bars demonstrate the same contribution but when the grid is shifted to achieve spatial oversampling.

FIG 8. Panel A: non-equilibrium response on a temperature jump of the surrounding environment: the outer shell become hotter, the inner shell is still cold, for the upward and the downward emitted signals (upper and lower rows, respectively). Panel B: equilibrated temperature difference response: hotter liposome signal minus cooler liposome signal, for the upward and the downward emitted signals (upper and lower rows, respectively). The image reconstruction is for an experiment when $\alpha = 38^{\text{o}}$.

FIG A1. Structural representations and $\{\Theta, \Phi\}$ angular dependencies of SFG nonlinearities. Upper and lower rows: mode #115 of all-trans decanoic acid and mode #114 of decanoic acid rotomer about the eighth carbon atom, respectively. The scale of the colour code is linear and varies in the range [-10, 10] from blue to red for all angular maps, save the chiral ones of the all-trans decanoic acid form, where the range is [-1, 1].

FIG B1. Left Side: deduced probabilities, according to Boltzmann distribution, for decanoic acid rotomers for the indicated temperatures according to the thermochemical output for use of Gaussian 09 (Frisch et al., 2010). Right Side: corresponding change of effective nonlinearities (Fig. 3) angular maps for upward and downward emitted signals.

REFERENCES

Angelova, M. & Dimitrov, D. (1986). Liposome electroformation. *Faraday Discuss. Chem. Soc.* **81**, 303-311.

Becke, D. (1988). Density-functional exchange-energy approximation with correct asymptotic behaviour. *Phys. Rev. A* **38**, 3098-3100.

Callender R.H. & Dyer, R.B. (2002). Probing protein dynamics using temperature jump relaxation spectroscopy. *Curr. Opin. Struct. Biol.* **12**, 628-633.

Chen, X., Hua, W., Huang, Z. & Allen, H. (2010). Interfacial Water Structure Associated with Phospholipid Membranes Studied by Phase-Sensitive Vibrational Sum Frequency Generation Spectroscopy. *J. Am. Chem. Soc.* **132**, 11336-11342.

Cimatu, K. & Baldelli, S. (2006). Sum Frequency Generation Microscopy of Microcontact-Printed Mixed Self-Assembled Monolayers. J. Phys. Chem. B **110**, 1807-1813.

Collazo, N., Shin, S. & Rice, S.A. (1992). Molecular-dynamics studies of the structure and properties of monolayers of perfluorinated amphiphiles. *J. Chem. Phys.* **96**, 4735-4742.

Dailey, C.A., Burke, B.J. & Simpson, G.J. (2004). The general failure of Kleinman symmetry in practical nonlinear optical applications. *Chem. Phys. Lett.* **390**, 8-13.

Dick, B., Gierulski, A., Marowsky, G. & Reider, G. A., (1985).Determination of the nonlinear optical susceptibility $\chi^{(2)}$ of surface layers by sum and difference frequency generation in reflection and transmission. *Appl. Phys. B* **38**, 107-116.

Djondjorova, P.A., Vassileva, V.M. & Mladenov, I.M. (2004). Analytic description and explicit parametrization of the equilibrium shapes of elastic rings and tubes under uniform hydrostatic pressure. *Int. J. Mech. Sci.* **53**, 355-364.

Felderhof, B.U. & Marowsky, G., (1987). Electromagnetic Radiation from a Polarization Sheet Located at an Interface Between Two Media. *Appl. Phys. B* **44**, 11-17.

Flörsheimer, M., Brillert, C. & Fuchs, H. (1999). Chemical Imaging of Interfaces by Sum Frequency Microscopy. *Langmuir* **15**, 5437-5439.

Frisch, M.J., Trucks, G.W., Schlegel, H.B., Scuseria, G.E., Robb, M.A., Cheeseman, J.R., Scalmani, G., Barone, V., Mennucci, B., Petersson, G.A., Nakatsuji, H., Caricato, M., Li, X., Hratchian, H.P., Izmaylov, A.F., Bloino, J., Zheng, G., Sonnenberg, J.L., Hada, M., Ehara, M., Toyota, K., Fukuda, R., Hasegawa, J., Ishida, M., Nakajima, T., Honda, Y., Kitao, O., Nakai, H., Vreven, T., Montgomery, J. A., Jr., Peralta, J. E., Ogliaro, F., Bearpark, M., Heyd, J.J., Brothers, E., Kudin, K. N., Staroverov, V.N., Kobayashi, R., Normand, J., Raghavachari, K., Rendell, A., Burant, J.C., Iyengar, S. S., Tomasi, J., Cossi, M., Rega, N., Millam, J. M., Klene, M., Knox, J. E., Cross, J. B., Bakken, V., Adamo, C., Jaramillo, J., Gomperts, R., Stratmann, R.E., Yazyev, O., Austin, A. J., Cammi, R., Pomelli, C., Ochterski, J. W., Martin, R. L., Morokuma, K., Zakrzewski, V.G., Voth, G.A., Salvador, P., Dannenberg, J.J., Dapprich, S., Daniels, A.D., Farkas, Ö., Foresman, J.B., Ortiz, J. V., Cioslowski, J. & Fox, D.J. (2010). *GAUSSIAN 09, Revision B.01*. Wallingford, CT: Gaussian, Inc.

Gros-Daillon, E., Maingault, L., Andre, L., Reboud, V., Verger, L., Charbon, E., Bruschini, C., Veerappan, C., Stoppa, D., Massari, N., Perenzoni, M., Braga, L. H. C., Gasparini, L., Henderson, R. K., Walker, R., East, S., Grant, L., Jatekos, B., Lorincz, E., Ujhelyi, F., Erdei, G., Major, P., Papp, Z. & Nemeth, G. (2013). First characterization of the SPADnet sensor: a digital silicon photomultiplier for PET applications. *IOP J. Instr.* **8**, C12026.

Gulliver, G. (1875). Observations on the sizes and shapes of the red corpuscles of the blood of the vertebrates with drawings of them to a uniform scale and extended and revised tables of measurements. *Proc. Zool. Soc. Lond.* **43**, 474-495.

Guyot-Sionnest, P., Hunt, H. & Shen, Y.R. (1987). Sum-frequency vibrational spectroscopy of a Langmuir film: Study of molecular orientation of a two-dimensional system. *Phys. Rev. Lett.* **59**, 1597-1600.

Han, Y., Raghunathan, V., Feng, R. Maekawa, H., Chung, C., Feng, Y., Potma, E.O. & Ge, N. (2013). Mapping Molecular Orientation with Phase Sensitive Vibrationally Resonant Sum-Frequency Generation Microscopy. J. Phys. Chem. B **117**, 6149-6156.

Hecht, E. (2002). *Optics*. San Francisco: Pearson Education Inc.

Hirose, C., Akamatsu, N. & Domen, K. (1992). Formulas for the Analysis of the Surface SFG Spectrum and Transformation Coefficients of Cartesian SFG Tensor Components. *Appl. Spec.* **46**, 1051-1072.

Hoffmann, D.M.P., Kuhnke, K. & Kern, K. (2002). Sum-frequency generation microscope for opaque and reflecting samples. *Rev. Sci. Instr.* **73**, 3221-3226.

Jang, J., Jacob, J., Santos, G., Lee, T. & Baldelli, S. (2013). Molecular Conformation as Contrast Mechanism in Sum Frequency Generation Microscopy. *J. Phys. Chem. C* **117**, 15192-15202.

Kleinman, D.A. (1962). Nonlinear Dielectric Polarization in Optical Media. *Phys. Rev.* **126**, 1977-1979.

Lee, C., Yang, W. & Parr, R. (1988). Development of the Colle-Salvetti correlation-energy formula into a functional of the electron density. *Phys. Rev. B* **37**, 785-789.

Li, G., Dhinojwala, A. & Yeganeh, M.S. (2011). Interference Effect from Buried Interfaces Investigated by Angular-Dependent Infrared−Visible Sum Frequency Generation Technique. *J. Phys. Chem. C* **115**, 7554-7561.

Li, G., Dhinojwala, A. & Yeganeh, M.S., (2011). Interference effect from buried interfaces investigated by angular-dependent infrared-visible sum frequency generation technique. *J. Phys. Chem. C* **115**, 7554–7561.

Moad, A.J. & Simpson, G.J. (2004). A Unified Treatment of Selection Rules and Symmetry Relations for Sum-Frequency and Second Harmonic Spectroscopies. *J. Phys. Chem. B* **108**, 3548-3562.

Nakano, T., Kikugawa, G. & Ohara T. (2010). A molecular dynamics study on heat conduction characteristics in DPPC lipid bilayer. *J. Chem. Phys.* **133**, 154705.

Phillips, C.M., Mizutani, Y. & Hochstrasser, R.M. (1995). Ultrafast thermally induced unfolding of RNase A. *Proc. Natl. Acad. Sci.* **92**, 7292-7296.

Potdar, D. & Sammalkorpi, M. (2015). Asymmetric heat transfer from nanoparticles in lipid bilayers. *Chem. Phys*. **463**, 22–29.

Schleeger, M, Nagata, Y. & Bonn, M. (2014). Quantifying Surfactant Alkyl Chain Orientation and Conformational Order from Sum Frequency Generation Spectra of CH Modes at the Surfactant-Water Interface. *J. Phys. Chem. Lett.* **5**, 3737-3741.

Sipe, J.E. (1981). The dipole antenna problem in surface physics: a new approach. *Surface Science* **105**, 489-504.

Staneva, G., Angelova, M. & Koumanov, K. (2004). Phospholipase A2 promotes raft budding and fission from giant liposomes. *Chem. Phys. Lipids.* **129**, 53-62.

Volkov, V. (2014). Tip-induced deformation of a phospholipid bilayer: Theoretical perspective of sum frequency generation imaging. *J. Chem. Phys.* **141**, 154201.

Volkov, V., Nuti, F., Takaoka, Y., Chelli, R., Papini, A.M. & Righini, R. (2006). Hydration and Hydrogen Bonding of Carbonyls in Dimyristoyl-Phosphatidylcholine Bilayer. *J. Am. Chem. Soc.* **128**, 9466-9471.

Walker, A., Conboy, J.C. & Richmond, G.L. (1997). Molecular Structure and Ordering of Phospholipids at a Liquid-Liquid Interface. *Langmuir* **13**, 3070-3073.

Xiao, D., Fu, L., Liu, J., Batista, V. & Yan, E, (2012). Amyloid Polypeptide Aggregates to Lipid/Aqueous Interfaces. *J. Mol. Biol.* **421**, 537-547.

Zhuang, X., Miranda, P.B., Kim, D. & Shen, Y.R., (1999). Mapping molecular orientation and conformation at interfaces by surface nonlinear optics. *Phys. Rev. B* **59**, 12632-12640.

Zhu, X.D., Suhr, H. & Shen, Y.R. (1987). Surface vibrational spectroscopy by infrared-visible sum frequency generation. *Phys. Rev. B* **35**, 3047-3050.
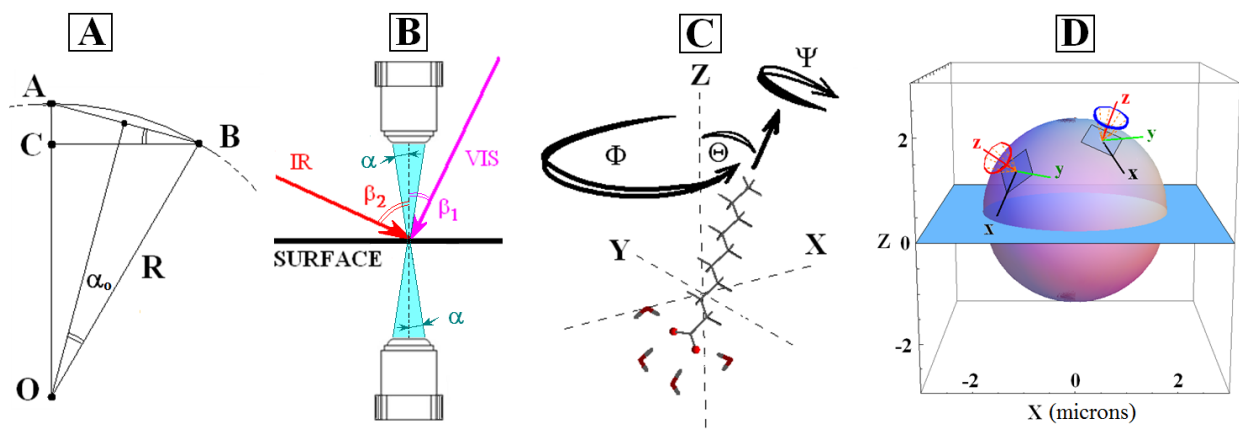
Figure 1.
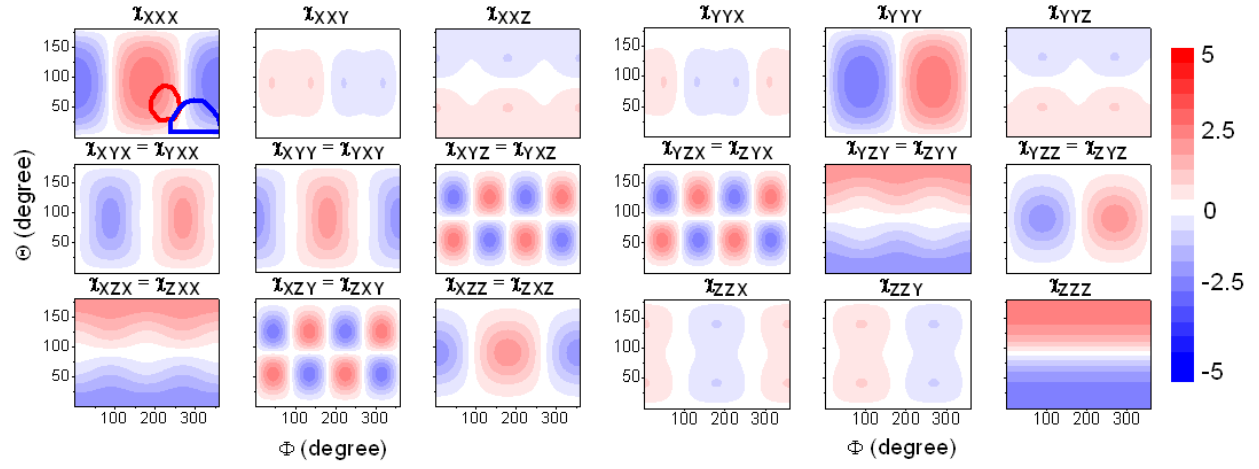
Figure 2.
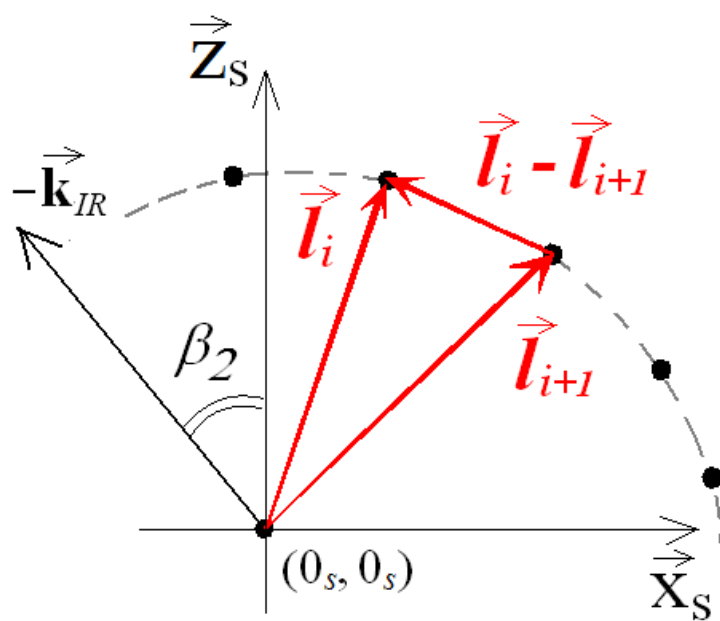
Figure 3.
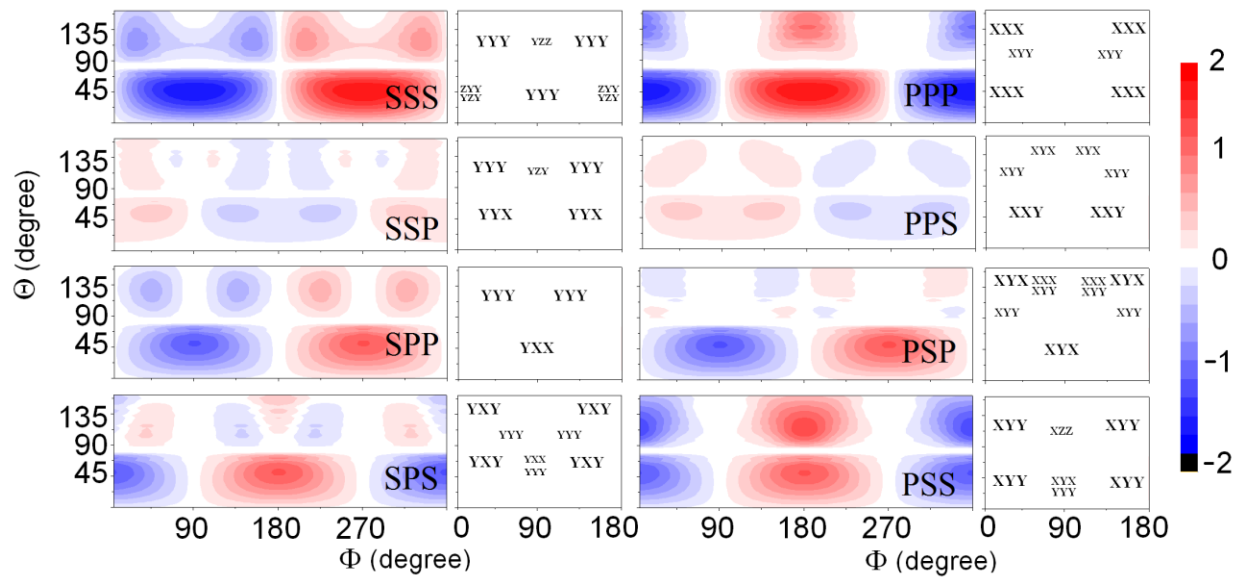
Figure 4.
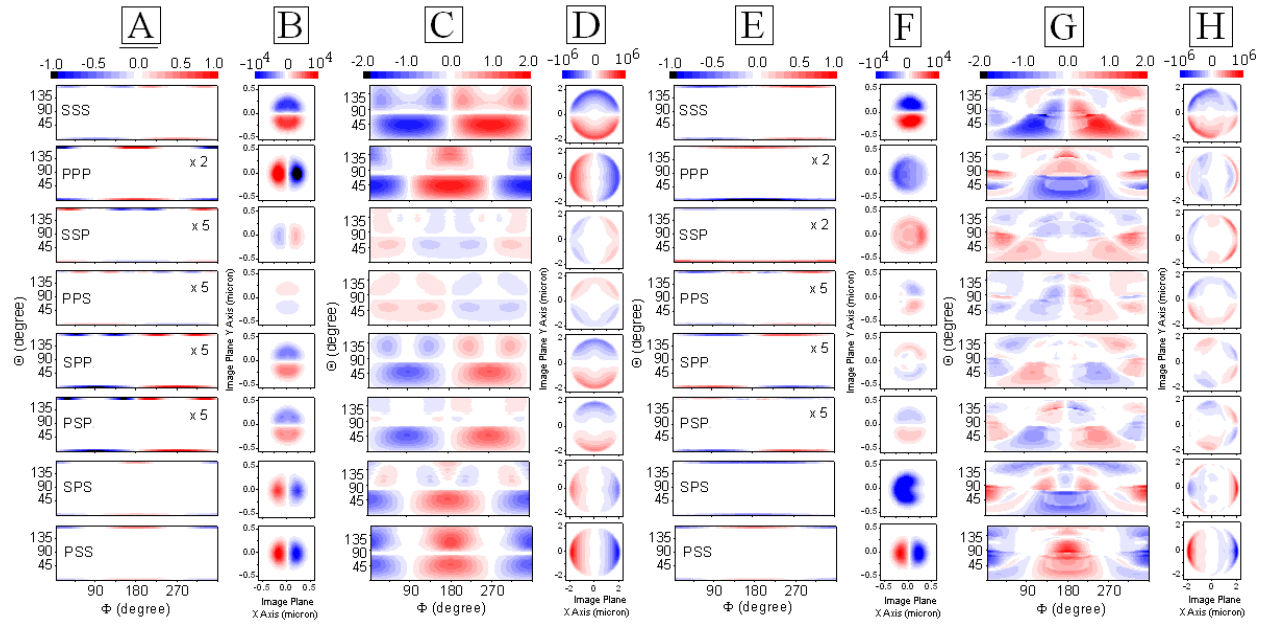
Figure 5.
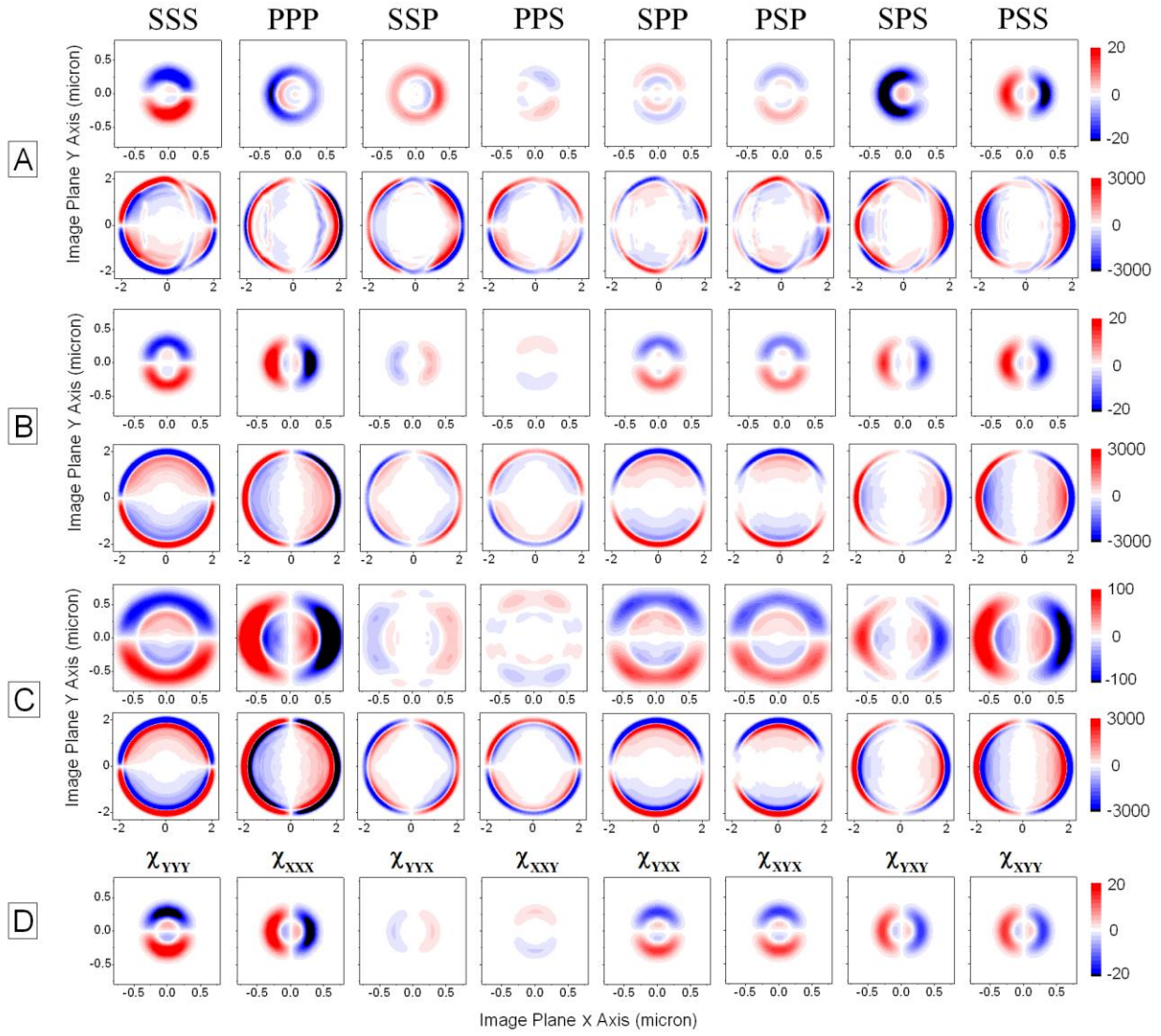
Figure 6.
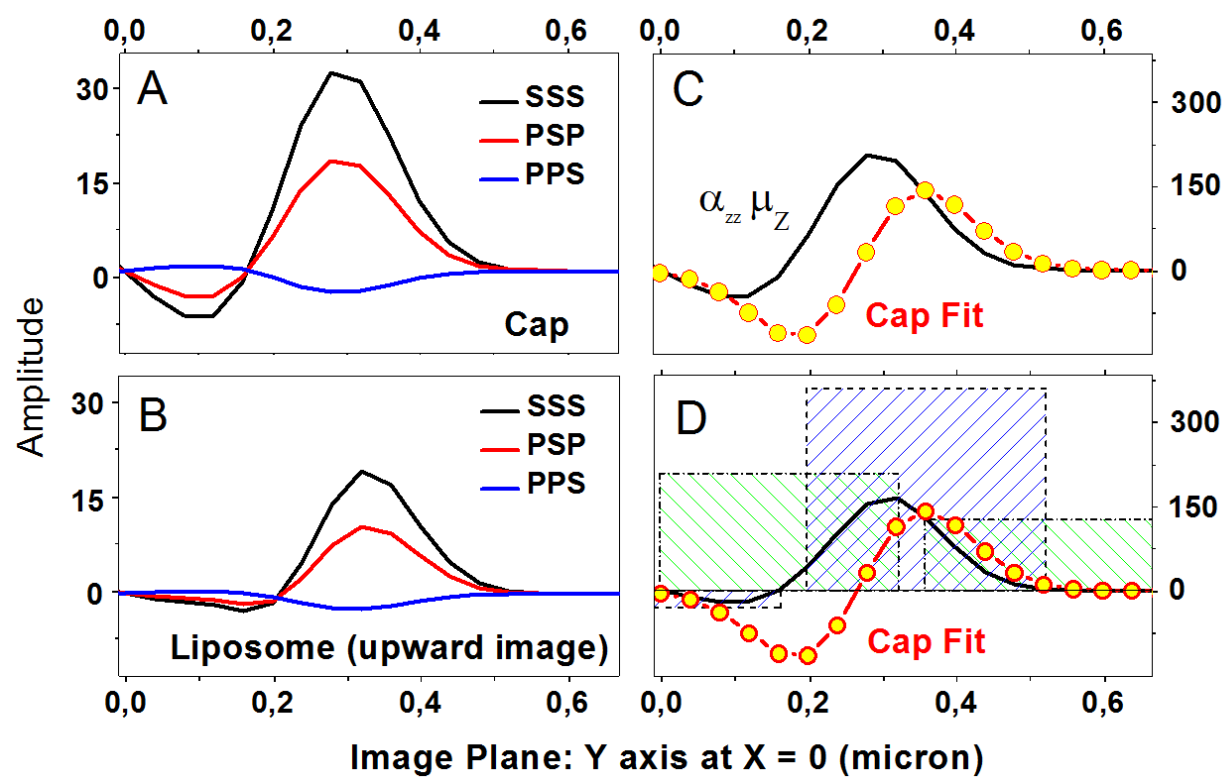
Figure 7.
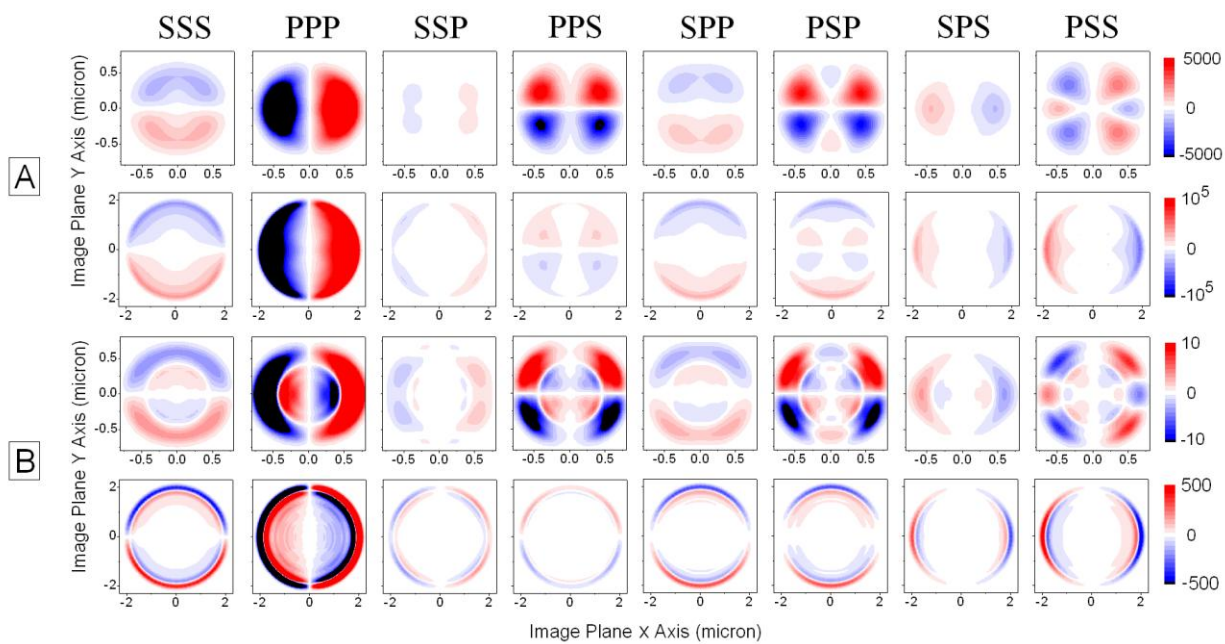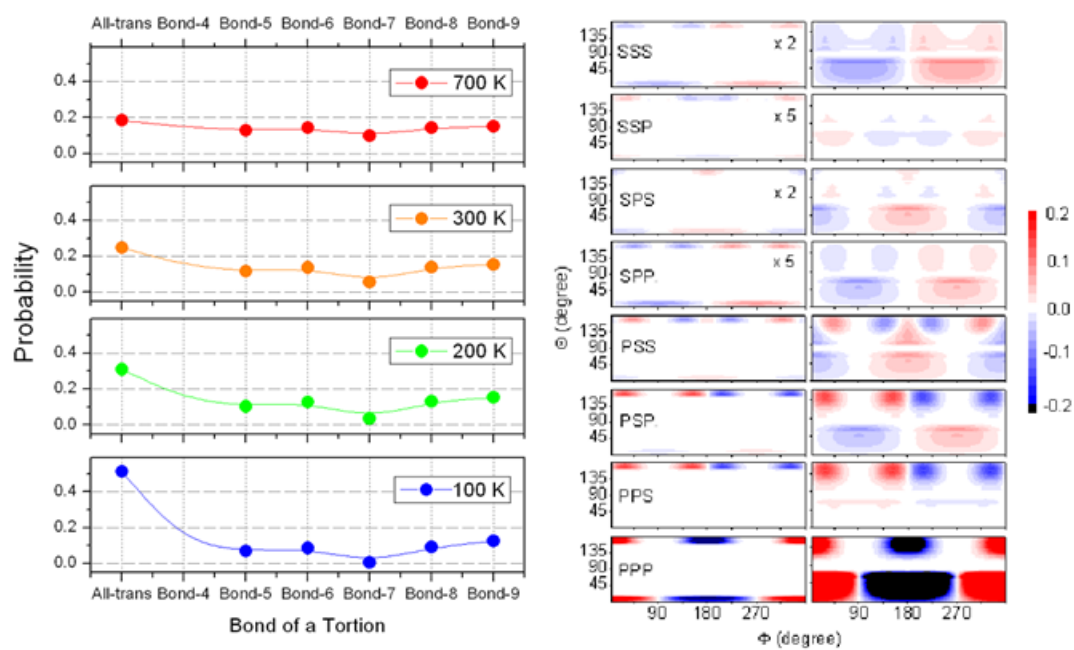
Figure 8.
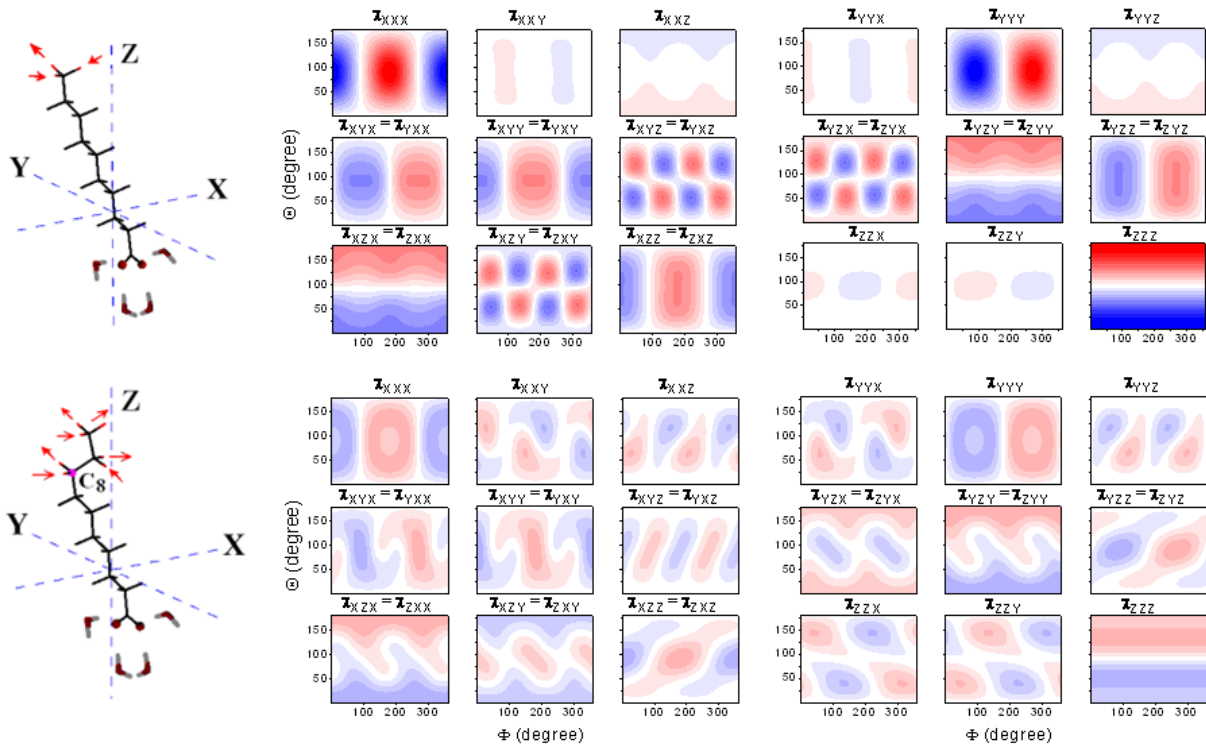
Figure A1.

Figure b1.

Supplementary Materials
Modeling of Infrared-Visible Sum-Frequency Generation
Microscopy Images of a Giant Liposome
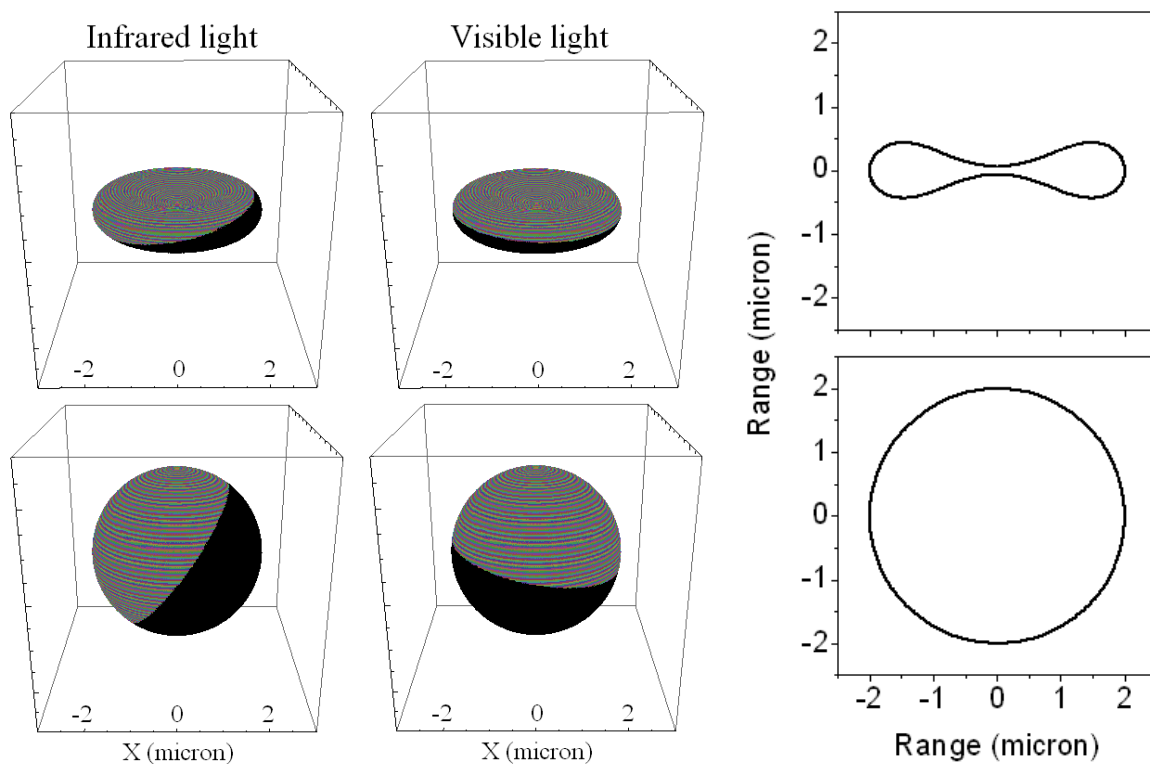
Victor Volkov, Carole C. Perry

Fig. S1. Left side: graphical presentations of sites sorted to be either under direct exposure (on the light side) or not (on the shadow side) at the interface of an elliptical biconcave object and a perfect sphere for Infrared and Visible beams under a non-degenerate experimental geometry, as shown in Fig. 1B in the article. Right side: profiles of the structures generated using the solution by Mladenov group (Djondjorova et al., 2004).
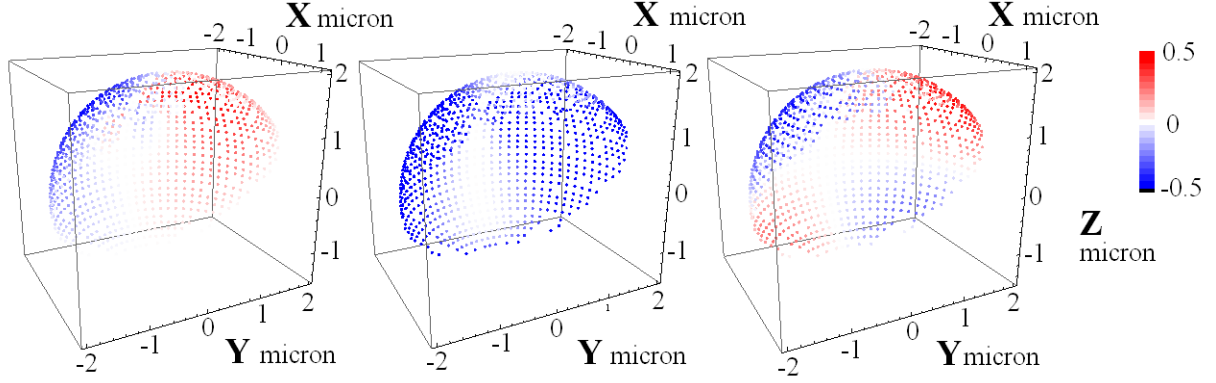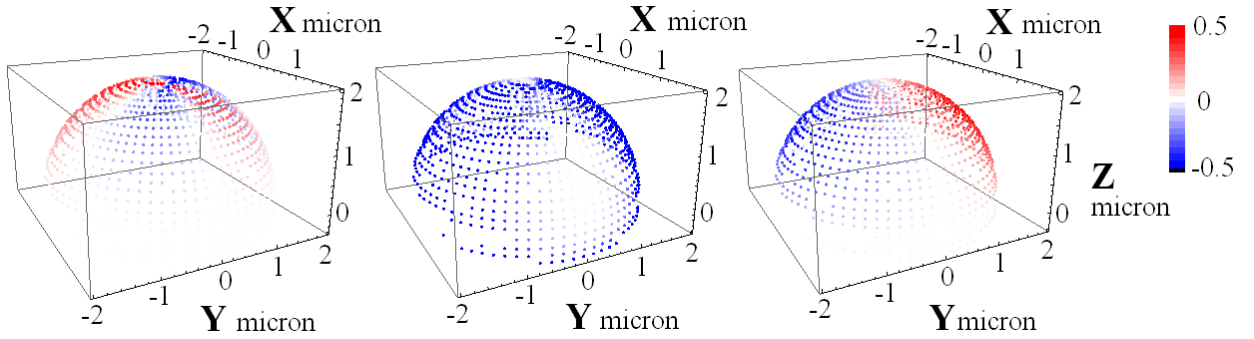
Fig. S2. Changes (gains or losses) of the S-polarized vector {0, 1, 0} in the laboratory frame of an IR beam upon passing sites at the surface side, under direct exposure to this field, under a non-degenerate geometry, when $\beta_1 \neq \beta_2$ according to Fig. 1B in the article. Panels from left to right: changes of the X, Y and Z components after transmission. Each site is represented by a small sphere colored according to a linearly scaled blue-white-red blend, the amplitudes of which is according to the minimum-maximum numerical values.

Fig. S3. Changes (gains or losses) of the S-polarized vector {0, 1, 0} in the laboratory frame of IR beam upon passing sites at the surface side under direct exposure to this field, under a degenerate geometry, when $\beta_1 = \beta_2$ according to Fig. 1B in the article. Panels from left to right: changes of the X, Y and Z components after transmission. Each site is represented by a small sphere colored according to a linearly scaled blue-white-red blend, the amplitudes of which is according to the minimum-maximum numerical values.

An example of the Mathematica code to express χ_{XXX} nonlinearity as a function of Φ and Θ angles:

```
B0 = RotationMatrix[(Pi / 2) - ψ, {0, 0, 1}]; C0 = RotationMatrix[θ, {-1, 0, 0}]; D0 = RotationMatrix[(Pi / 2) + φ, {0, 0, -1}];
D3A = Transpose[B0.C0.D0];
RTz = ( xx xy xz )
      ( yx yy yz ); TDM = {X, Y, Z};
      ( zx zy zz )
(*XXX: 1 for X, 2 for Y, 3 for Z*)
B1 = 1; B2 = 1; B3 = 1;
F[φ_, θ_, ψ_] := Sum[D3A[[B1, ic]] * Sum[D3A[[B2, jc]] * RTz[[ic, jc]], {jc, 1, 3}], {ic, 1, 3}] * Sum[D3A[[B3, kc]] * TDM[[kc]], {kc, 1, 3}];
TMP = Integrate[F[φ, θ, ψ], {ψ, 0, 2 Pi}];
XXX[φ_, θ_] := Sin[θ] * TMP
```

$\frac{1}{8}$ π Cos[φ] (6 X xz + 6 Y yz + 6 xx Z + 6 yy Z + 6 X zx + 6 Y zy + 4 Z zz + 2 (X (xz + zx) + Y (yz + zy) + Z (xx + yy − 2 zz)) Cos[2 θ] +

(X (xz + zx) + Y (yz + zy) + Z (xx + yy − 2 zz)) Cos[2 (θ − φ)] − 2 X xz Cos[2 φ] − 2 Y yz Cos[2 φ] − 2 xx Z Cos[2 φ] − 2 yy Z Cos[2 φ] − 2 X zx Cos[2 φ] − 2 Y zy Cos[2 φ] +
4 Z zz Cos[2 φ] + X xz Cos[2 (θ + φ)] + Y yz Cos[2 (θ + φ)] + xx Z Cos[2 (θ + φ)] + yy Z Cos[2 (θ + φ)] + X zx Cos[2 (θ + φ)] + Y zy Cos[2 (θ + φ)] − 2 Z zz Cos[2 (θ + φ)]) Sin[θ]²

Multiplication with a sine function is according to the numerator integral in Equation A1 in Appendix A.

Comparisons of results of approximate expressions received upon "rotations to angles" (solid red line) with the outcomes of exact integrations (black dots), for nonlinearity χ_{XXX}.

```
(*Raman Tensor*)
       ( −0.0440298  −0.355241   0.0861879  )
RTz = (  −0.355241   −0.0376467  0.00322857 );
       (  0.0861879   0.00322857 −0.015312   )
(*setting the components of the Raman Tensor*)
( xx xy xz )
( yx yy yz ) = RTz;
( zx zy zz )
(*Transition Dipole Moment*)
TDM = {8.74059, −0.096396, −0.0584377};
(*setting the components of the Transition Dipole Moment*)
{X, Y, Z} = TDM;
(*Nonlinear Susceptibility of Interests as a function of Euler angles: Fi and Theta*)
XXX[φ_, θ_] :=
    1
    ─ π Cos[φ] (6 X xz + 6 Y yz + 6 xx Z + 6 yy Z + 6 X zx + 6 Y zy + 4 Z zz +
    8
        2 (X (xz + zx) + Y (yz + zy) + Z (xx + yy − 2 zz)) Cos[2 θ] +
        (X (xz + zx) + Y (yz + zy) + Z (xx + yy − 2 zz)) Cos[2 (θ − φ)] − 2 X xz Cos[2 φ] −
        2 Y yz Cos[2 φ] − 2 xx Z Cos[2 φ] − 2 yy Z Cos[2 φ] − 2 X zx Cos[2 φ] − 2 Y zy Cos[2 φ] +
        4 Z zz Cos[2 φ] + X xz Cos[2 (θ + φ)] + Y yz Cos[2 (θ + φ)] + xx Z Cos[2 (θ + φ)] +
        yy Z Cos[2 (θ + φ)] + X zx Cos[2 (θ + φ)] + Y zy Cos[2 (θ + φ)] − 2 Z zz Cos[2 (θ + φ)]) Sin[θ]²;
```

ROTATION TO ANGLES APPROACH:

we may set Fi angle to zero and vary calculate the expression of this function according to any desired Theta.
There should be the correspondent normalization scaling factor

$$B = \text{Plot}\left[\frac{1}{2\,\text{Pi} * \text{Sin}[\theta]} \, \text{XXX}[0, \theta], \{\theta, 0, \text{Pi}\}, \text{PlotStyle} \to \text{Red}\right];$$

(*This red-line plot will be shown at the end*)

EXACT INTEGRATIONS

(***Fi-angle setting:** we will take 1-degree interval about Fi=0 *)

FiAg = 0;

$$\text{FL} = \frac{\text{Pi}}{180} \, \{\text{FiAg} - 0.5, \text{FiAg} + 0.5\};$$

(***Theta-angle space:** setting the central angles*)

dimθ = 251;   (*number of theta angles to sample*)

ThStp = 0.72 ; (*Angular step ,degrees*)

tht = Table[i * ThStp - ThStp, {i, 1, dimθ}];

(*Theta space integration intervals*)

LM1 = Table[{0, 0}, {l, 1, dimθ}];

N1 = dimθ - 1;

Do[LM1[[l, 1]] = 0.5 * (tht[[l]] + tht[[l - 1]]);

  LM1[[l, 2]] = 0.5 * (tht[[l]] + tht[[l + 1]]), {l, 2, N1}];

LM1[[1, 2]] = LM1[[2, 1]];

LM1[[N1 + 1, 1]] = LM1[[N1, 2]];

LM1[[N1 + 1, 2]] = 180;

(*conversion to radians*)

$$\text{LM1} = \frac{\text{Pi}}{180} \, \text{LM1};$$

(*Developing the normalization factors for the Fi and Theta intervals*)

NFF[θ_] := Integrate[Integrate[Sin[θ], {ψ, 0, 2 Pi}], {ϕ, FL[[1]], FL[[2]]}]

NF = Table[0, {l, 1, dimθ}];

Do[NF[[i]] = Integrate[NFF[θ], {θ, LM1[[i, 1]], LM1[[i, 2]]}], {i, 1, dimθ}] //
  AbsoluteTiming

(***Integration about the Fi-angle interval**)

Integrate[XXX[ϕ, θ], {ϕ, FL[[1]], FL[[2]]}]

OFN[θ_] := 0.0414695 * Sin[θ]^2 - 0.0413693 * Sin[θ]^4 + 0.0103423 * Sin[2 θ]^2

(*Integrations about the Theta-angle intervals*)

DAT = Table[0, {l, 1, dimθ}];

Do[lt1 = LM1[[l, 1]]; lt2 = LM1[[l, 2]];

  DAT[[l]] = Integrate[OFN[th], {th, lt1, lt2}];

  Clear[lt1, lt2], {l, 1, dimθ}] // AbsoluteTiming

(*Normalization*)

Do[DAT[[l]] = DAT[[l]] / NF[[l]], {l, 1, N1 + 1}];

(*Comparison to the approach by Rotation to angles*)

A = ListPlot$\left[\text{Table}\left[\left\{i \, \frac{Pi}{251}, \, DAT[[i]]\right\}, \{i, 1, 251\}\right]\right]$;

Show[A, B]